Acta Pharmaceutica Sinica B 2026;16(5):3224−3242

Chinese Pharmaceutical Association
Institute of Materia Medica, Chinese Academy of Medical Sciences

Acta Pharmaceutica Sinica B

www.elsevier.com/locate/apsb
www.sciencedirect.com

ORIGINAL ARTICLE

Biomimetic liposomes synergize with high-intensity focused ultrasound to induce ferroptosis in tumors

Ruizhe Xu[a], Xuejing Li[a], Xiaomin Su[a], Xifeng Qin[a], Ying He[a], Siyu Wang[a], Yue Liu[a], Jiayi Wu[a], Ting Wang[a], Mingyang Liu[d], Boshu Ouyang[e], Jia Li[f], Wuli Yang[c], Bo Zhang[b,*], Zhiqing Pang[a,*]

[a]*School of Pharmacy, Fudan University, Key Laboratory of Smart Drug Delivery, Ministry of Education, State Key Laboratory of Advanced Drug Formulations for Overcoming Delivery Barriers, Shanghai 201203, China*
[b]*Institute of Hematology, Union Hospital, Tongji Medical College, Huazhong University of Science & Technology, Wuhan 430022, China*
[c]*State Key Laboratory of Molecular Engineering of Polymers & Department of Macromolecular Science, Fudan University, Shanghai 200433, China*
[d]*Key Laboratory of Precision Diagnosis and Treatment of Gastrointestinal Tumors, China Medical University, Ministry of Education, Shenyang 110001, China*
[e]*Department of Integrative Medicine, Huashan Hospital, Fudan University, Shanghai 200040, China*
[f]*Department of Biomedical Sciences, Faculty of Medicine, Health and Human Sciences, Macquarie University, Sydney, NSW 2109, Australia*

Received 8 January 2025; received in revised form 28 July 2025; accepted 28 July 2025

KEY WORDS

High intensity focused ultrasound;
Ferroptosis therapy;
Gambogic acid;
Biomimetic liposomes;
Drug delivery;
Breast cancer;
Cancer therapy;
Nanomedicine

Abstract The efficient targeted delivery and on-demand release of nanomedicines still present significant challenges in tumor therapy. In the present study, we developed a novel strategy of tumor ferroptosis therapy through the synergistic effect of nanomedicines (biomimetic liposomes) and a medical device (high-intensity focused ultrasound, HIFU). It was found that HIFU irradiation induced heightened expressions of CD44 and reactive oxygen species (ROS) in tumor cells by 1.43-fold and 2.64-fold, respectively. This allowed the gambogic acid-loaded, platelet-mimicking liposomes (PLip) to more precisely target the tumor cells through the interaction of CD44 and P-selectin on the PLip and subsequently ROS-responsively release the drug from PLip, thus effectively killing tumor cells. Crucially, gambogic acid

*Corresponding authors.
E-mail addresses: zhangbo19871987@126.com (Bo Zhang), zqpang@fudan.edu.cn (Zhiqing Pang).

Peer review under the responsibility of Chinese Pharmaceutical Association and Institute of Materia Medica, Chinese Academy of Medical Sciences.

https://doi.org/10.1016/j.apsb.2026.02.024

also significantly enhanced ROS production, leading to lipid peroxidation and augmented ferroptosis induced by HIFU. In summary, HIFU demonstrates immense potential in synergizing with nanomedicines to combat tumors.

1. Introduction

Over the past few decades, there has been a significant increase in targeted delivery methods for cancer treatment, typically involving the systemic administration of therapeutic drugs encapsulated in nanocarriers (NCs) or the localized delivery of these nanomedicines to affected tissues. These nanomedicines are designed to enhance drug concentration in tumor tissues, extend circulation time, and reduce toxicity to normal tissues, thereby improving therapeutic efficacy and safety[1−3]. However, compared to a multitude of successful preclinical studies, only over 90 nanomedicines have been approved for clinical use[4]. An analysis of preclinical data on NC-based tumor delivery platforms revealed that less than 0.7% (%ID, median) of the nanomedicines accumulated within tumors[5]. Low specificity to tumors is a common issue with nanomedicines, which weakens the tumor accumulation and cellular internalization. To augment the targeting capability of nanomedicines, nanomedicines are frequently surface-modified with molecules possessing specific affinity, such as aptamers, proteins, and small molecules. These molecules can bind to receptors on the surface of tumor cells, thus enhancing the uptake and absorption of therapeutic agents. Researchers also integrate these systems with external techniques like ultrasound[6,7], hyperthermia[8,9], and radiation[10,11] to alter tumor interstitial fluid pressure, vascular permeability, and density, thereby enhancing permeability. Additionally, studies are exploring the use of ultrasound[12−15] and magnetic fields[16,17] to directly manipulate the movement of nanomedicines, a promising strategy to improve the accumulation of nanocarriers at tumor sites, further enhancing targeting capability.

Moreover, these tumor-accumulated nanomedicines need to be effectively internalized by tumor cells. To maximize therapeutic effect, nanomedicines also require controlled drug release at the target site, and numerous studies have focused on nanoplatforms responsive to tumor-specific microenvironmental stimuli such as pH[18], reactive oxygen species (ROS)[19], glutathione[20], adenosine triphosphate[21], enzymes[22], and inflammatory factors[23]. However, the heterogeneity of the tumor environment frequently results in variability in the effectiveness of drug release[24]. Meanwhile, the limited sensitivity and release efficiency of these nanomedicines are significant disadvantages. Additionally, certain functionalized nanoparticles can be activated by external stimuli like magnetic fields[25], light[20], and ultrasound[26,27], enabling effective tumor-controlled drug release in a time- and space-specific manner[28]. Nevertheless, most methods for controlling drug release using external stimuli do not possess the capability to enhance the drug's activity. Therefore, it is necessary to develop strategies to effectively release drugs from nanomedicines and even enhance the drug activity to maximize their anti-tumor efficacy.

High-intensity focused ultrasound (HIFU) is a non-invasive therapeutic technique that uses focused ultrasound waves to destroy cancerous tissues with precision. This innovative technology has shown great promise not only in cancer ablation therapy by offering a targeted treatment option that minimizes damage to surrounding healthy tissues, but also in cancer drug delivery to enhance targeted drug delivery. HIFU can disrupt or temporarily open the blood−brain barrier[29,30] and other biological barriers[31,32], facilitating the delivery of therapeutic agents to previously inaccessible areas. Additionally, HIFU induces the formation of transient pores on cell membranes[32], significantly boosting cellular uptake of drugs. Existing research has demonstrated that HIFU irradiation significantly elevates the levels of ROS at tumor sites[33−36], which will facilitate an efficient ROS-responsive release of drugs from nanomedicines at the tumor site. Recently, we found that HIFU could induce tumor cell ferroptosis through regulating the expression of ferroptosis-associated genes[37]. Consequently, HIFU can be leveraged as an external technique to directly alter the tumor microenvironment and regulate tumor cell gene expression. This alteration may potentially enhance targeted tumor drug delivery, responsive drug release, and boost the antitumor efficacy of drugs, while the drug itself may amplify the destructive impact of HIFU.

Based on the above theoretical analysis, we have developed a novel strategy of tumor ferroptosis therapy through the synergistic effect of nanomedicines (biomimetic liposomes) and the medical device HIFU (Fig. 1). Gambogic acid (GA)-loaded platelet-like liposomes (PLip) were designed for the treatment of basal-like breast cancer. HIFU irradiation was used to induce upregulated expressions of CD44 receptors on tumor cells and ROS generation in tumor cells, which could promote PLip's tumor-targeted delivery through the interaction of CD44 and P-selectin on the PLip and subsequent intracellular ROS-responsive release of drug from PLip. Furthermore, the high accumulation of the drug in tumor cells, in turn, enhanced the ferroptosis effect triggered by HIFU. We carefully assessed the augmented anti-tumor efficacy and the underlying mechanism of PLip in combination with HIFU in an orthotopic tumor model of basal-like breast cancer. This study presented new strategies for combining nanomedicines and medical devices for solid tumor treatment, aiming to maximize therapeutic outcomes.

2. Materials and methods

2.1. Materials

RPMI-1640 medium (PWL004), 1% (*v*/*v*) penicillin/streptomycin (MA0110), trypsin (MA0233), and fetal bovine serum (FBS, PWL040) were purchased from MeilunBio (Dalian, China). Ethylenediaminetetraacetic acid disodium salt (EDTA-2Na, AR250G) and 3% hydrogen peroxide (H_2O_2, GR 500 mL) were obtained from SINOPHARM (Beijing, China). Cholesterol (O01001) and 1,2-distearoyl-*sn*-glycero-3-phosphoethanolamine-*N*-[succinyl(polyethylene glycol)-2000] (DSPE-PEG, F09001)

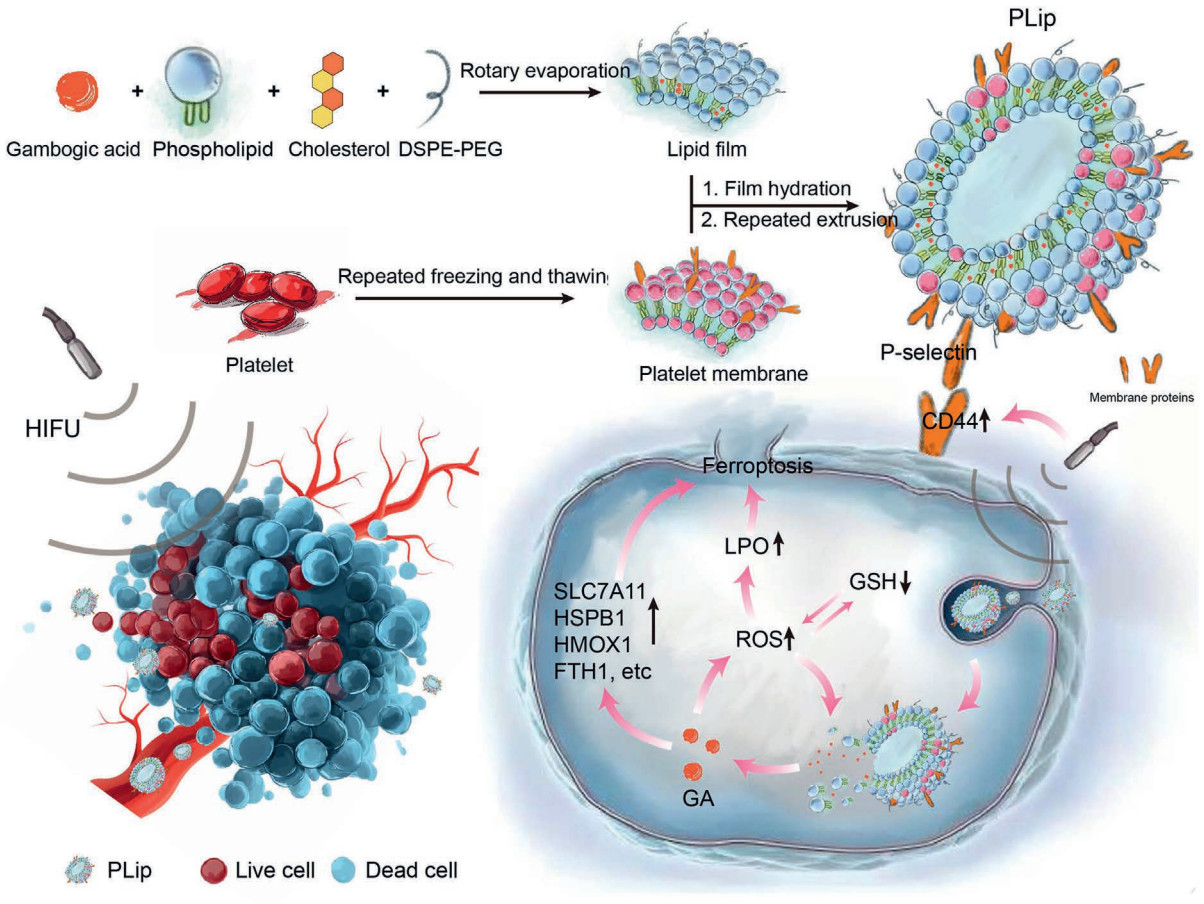

Figure 1 Preparation process of platelet biomimetic liposomes and their mechanism in promoting HIFU-induced ferroptosis.

were from AVT (Shanghai, China). prostaglandin E1 (PGE1, P850066) was acquired from MACKLIN (Shanghai, China). Egg yolk lecithin (PC-98T) was purchased from Kewpie (Tokyo, Japan). Protease inhibitor (87786) was from ThermoFisher Scientific (Waltham, MA, USA). Gambogic acid (GA, G101480) was obtained from Aladdin (Shanghai, China). CD44 antibody (KM201) was from Abcam (Cambridge, Cambridgeshire, UK). Cell counting kit-8 (CCK-8, BS350A) was purchased from Biosharp (Hefei, Anhui, China). 2-(4-Amidinophenyl)-6-indolecarbamidine dihydrochloride (DAPI, C1002), Annexin V-FITC/PI cell apoptosis kit (C1062M), and the reduced/oxidized glutathione (GSH/GSSG) assay kit (S0053) were from Beyotime Biotechnology (Shanghai, China). Eosin (318906), hematoxylin (H3136), and bovine serum albumin (BSA, V900933) blocking solution were from Sigma−Aldrich (St. Louis, MO, USA). The *in situ* cell death detection kit (Cat. No.11684817910) was from Roche Diagnostics (Basel, Switzerland). ProLong® Gold Antifade Reagent with DAPI (C1002) and 2′,7′-dichlorodihydrofluorescein diacetate (DCFH-DA, S0033S) were also from Beyotime Biotechnology (Shanghai, China). C11 BODIPY 581/591 (GC40165) was from GLPBIO (Montclair, CA, USA). ROSGreen™ H_2O_2 Probe (MX5202-1 MG) was purchased from Maokang Biotechnology Co. (Shanghai, China). Alexa Fluor® 568 Goat Anti-Rabbit IgG (A-11008) was obtained from Invitrogen (Carlsbad, CA, USA). The ferrous ion fluorescent probe FerroOrange (F374) was from Dojindo Laboratories (Kumamoto, Japan). Ferrostatin-1 (Fer-1, HY-100579), deferoxamine (DFO, HY-B1625), and vitamin E (Ve, HY-N0683) were from MedChemExpress (Monmouth Junction, NJ, USA). The cellulose ester dialysis membrane (SP131264) was purchased from Yuanye Bio-Technology (Shanghai, China).

2.2. *Cells and animals*

The murine mammary carcinoma cells, 4T1 cell lines as model basal-like breast cancer cells, were procured from the American Type Culture Collection (ATCC). These cells were cultured in RPMI-1640 medium supplemented with 10% FBS and 1% penicillin/streptomycin, in an environment maintained at 37 °C and 5% CO_2. Six-week-old female BALB/c mice were obtained from SLAC Animal Co., Ltd. (Shanghai, China). These mice were housed in groups of six mice per cage in a controlled environment, with a temperature maintained at approximately 22 ± 2 °C and a 12-h light cycle from 08:00 to 20:00. They were provided with a standard diet and water. All experimental protocols were carried out in accordance with the guidelines approved by the Ethics Committee of Fudan University (2024-03-YJ-PZQ-65).

2.3. *Determination of the ferroptosis inducer*

Expression levels of typical ferroptosis-related genes in human breast cancer subtypes were retrieved from the TIMER database (http://timer.comp-genomics.org/timer/), and the expressions of 25 genes were found to be significantly different. Ferroptosis is a cell

death process driven by iron-dependent oxidative stress. Oxidative stress can directly cause ferroptosis, and ferroptosis can further enhance oxidative stress, creating a vicious cycle[38,39]. Thioredoxin (TXN) is a protein that plays a critical role in protecting cells from oxidative stress by maintaining redox balance[40] and regulating relevant signal pathways[41]. Myeloid cell leukemia-1 (MCL-1) is a crucial protein in controlling apoptosis. However, certain studies have indicated that it may impact the generation of reactive oxygen species (ROS) *via* a ferroptosis-related protein known as NOX4[42]. Thus, the regulation of these two proteins can be employed to control the oxidative stress environment in tumors and ultimately augment the process of ferroptosis in tumor cells. The expression patterns for TXN and MCL1 genes across various breast cancer subtypes and normal tissues involved the retrieval of RNA-sequencing expression profiles (level 3) and clinical data for breast cancer from the TCGA dataset (https://portal.gdc.com). Additionally, the latest release (V8) GTEx datasets was acquired from the GTEx data portal (https://www.gtexportal.org/home/datasets). Statistical analyses were conducted using R software v 4.0.3 (R Foundation for Statistical Computing, Vienna, Austria), with significance determined at P-value <0.05. Using the Timer2 database, correlations of the gene expressions between these 25 ferroptosis-related genes and TXN (or MCL1) in four breast cancer tumor subtypes were also discovered. Protein−protein interaction networks were constructed by querying 25 ferroptosis-related genes, TXN, and MCL1 genes using the STRING database (https://string-db.org). The protein targets of gambolic acid, TXN and MCL1, were identified using the SwissTargetPrediction database (https://www.swisstargetprediction.ch) and the Comparative Toxicogenomics database (CTD, https://ctdbase.org/). The production of molecular docking diagrams between gambogic acid and TXN, MCL1 involved initially obtaining protein 3D structures from the RCSB PDB database (https://www.rcsb.org) and gambogic acid molecule 3D structures from the NCBI database (https://www.ncbi.nlm.nih.gov/). Subsequently, Molecular Viewer (v 1.5.7) and Autodock Vina (v 1.1.2) were employed to acquire the optimal molecular conformations for the docking process. Ultimately, visualization was accomplished using Pymol (v 2.4).

2.4. Preparation and characterization of platelet-biomimetic liposomes (PLip)

Following the extraction of nonactivated platelets (PLT) from BALB/c mice, platelet membranes were obtained by repeating freezing and thawing[43]. This involved freezing the PLT in liquid nitrogen and then thawing it at room temperature, a process that was repeated for ten cycles. Following this, the PLT membrane was collected by centrifuging at 10,000 × g for 10 min. The preparation process for gambogic acid-loaded platelet-biomimetic liposomes was carried out using the thin-film dispersion method as previously described[44,45]. Briefly, 4 mg of egg yolk lecithin, 1 mg of cholesterol, 0.4 mg of DSPE-PEG, and 0.52 mg of GA were dissolved in 5 mL of dichloromethane. The dichloromethane was then evaporated to form a lipid film. Subsequently, platelet membranes extracted from 2 mL of BALB/c mouse blood was added, along with PBS to make up a total volume of 2.7 mL. This mixture was stirred for an hour. The resulting solution was successively extruded 20 times through polycarbonate filters of 200 nm and 100 nm to obtain gambogic acid-loaded platelet biomimetic liposomes (PLip). The same method was used to prepare PEGylated liposomes (Lip) without the addition of platelet membranes. The same method was also used to prepare blank PLip without the addition of GA. For the preparation of DiD-labeled liposomes, 10.8 μg of DiD was added to the organic phase before evaporation to form a lipid film. The subsequent steps remained unchanged, allowing for the production of both DiD-labeled PLip (DiD-PLip) and DiD-labeled Lip (DiD-Lip).

To characterize liposomes, the prepared liposomes were diluted 100 times and then analyzed by dynamic light scattering (DLS) with a Zetasizer Nano-ZS analyzer (Malvern Panalytical Ltd., Malvern, Worcestershire, UK). This process measured the average particle size, polydispersity index (PdI), and zeta potential of the particles. Concurrently, measurements were taken for platelet membrane vesicles (PLA), PLip, Lip, and blank PLip. Additionally, PLip was stored at 4 °C over a period of seven days and the particle size and PdI were measured every day to assess their stability *in vitro*. The morphology of PLip was visualized by cryogenic electron microscopy (Cryo-EM, JEOL 2100; JEOL Ltd., Tokyo, Japan) as previously described[46,47].

To quantify the drug loading capability (DLC) and encapsulation efficiency (EE), PLip and Lip were centrifuged at 100,000 × g for 30 min in an ultracentrifuge (CP100NX; HITACHI, Japan) to remove the supernatant. The resulting pellet was dissolved in 1 mL of methanol, and the absorbance at 360 nm was measured to quantify the concentration of GA using a UV spectrophotometer (Cary 6000i UV−Vis−NIR; Agilent, Santa Clara, CA, USA). DLC and EE were calculated using the provided Eqs. (1) and (2).

$$\text{DLC} = (\text{Mass of drug encapsulated in liposomes} / \text{Mass of liposomes}) \times 100\% \quad (1)$$

$$\text{EE} = (\text{Mass of drug encapsulated in liposomes} / \text{Mass of drug input}) \times 100\% \quad (2)$$

2.5. Validation of PLip enhancing HIFU-induced ferroptosis in vitro

Ferroptosis inhibitors like Vitamin E (Ve), the iron chelator Deferoxamine (DFO), and Ferrostatin-1 (Fer-1) were selected to validate HIFU + PLip-induced ferroptosis. Briefly, 4T1 cells were seeded into a 12-well plate and cultured overnight. After trypsin digestion and collection, the cells were treated with 8.5 W HIFU (CZF-200; Chongqing Haifu Technology, Chongqing, China) for 30 s. Afterward, cells were incubated with PLip (0.5 μg/mL of GA) in the presence or absence of different ferroptosis inhibitors, including Ve (40 μmol/L), DFO (100 μmol/L), or Fer-1 (10 μmol/L). 24 h later, the cell viability was measured using the CCK-8 assay according to the routine protocol. Concurrently, cells underwent HIFU, PLip, or PBS treatment served as controls.

Additional measurements were carried out to evaluate alterations of typical ferroptosis-related markers within cells following HIFU + PLip treatment, such as ROS, Fe^{2+}, lipid peroxidation (LPO), and glutathione (GSH). In brief, 4T1 cells were cultured on 12-well chamber slides overnight. The cells were then collected, resuspended in 1 mL of culture medium, and irradiated with 8.5 W HIFU for 30 s before coincubation with PLip (0.5 μg/mL of GA). For ROS measurement, after 2-h coincubation, cells were stained with DCFH-DA at 37 °C for 20 min, followed by nucleus staining with DAPI for 15 min, and then analyzed for ROS content using a flow cytometer (BD

FACSCanto™ II; BD Biosciences, East Rutherford, NJ, USA) and a fluorescence confocal microscope (FV31S-SW; Olympus, Tokyo, Japan). For LPO measurement, after 12 h coincubation, cells were incubated with the LPO probe C11-BODIPY at 37 °C for 30 min, followed by nucleus staining with DAPI for 15 min, and the LPO content was monitored using flow cytometry and a fluorescence confocal microscope. For iron content analysis, after 12-h coincubation, cells were stained with FerroOrange for 30 min followed by nucleus staining with DAPI for 15 min, and analyzed using flow cytometry and a fluorescence confocal microscope. For GSH measurement, after 12 h of coincubation, intracellular GSH content was measured according to the protocol of the GSH/GSSG assay kit. Cells treated solely with HIFU, PLip, or PBS served as controls.

2.6. HIFU enhanced the uptake of platelet-biomimetic liposomes by tumor cells in vitro

4T1 cells were seeded into a 12-well plate and cultured overnight. After 24 h, the cells were digested with trypsin, centrifuged, and then resuspended in 1 mL of culture medium. After HIFU irradiation at a power of 8.5 W for 30 s, DiD-labeled PLip and Lip were added to the culture medium at a final concentration of 2 μg/mL. At the same time, the same concentration of DiD-PLip and DiD-Lip was added to cells without HIFU irradiation. After 2 h, the fluorescence intensity of cells was measured using flow cytometry (BD Biosciences). To observe the cellular uptake more intuitively, cell nuclei were stained with DAPI for observation under a fluorescence confocal microscope (Olympus).

To explore how HIFU boosts cellular uptake, we assessed the level of CD44 protein expression on 4T1 cells, which serves as the receptor for P-selectin on PLip, using Western blot (WB) analysis both before and after exposure to HIFU. In brief, 4T1 cells were seeded in a 6-well plate, cultured overnight, and subjected to HIFU treatment (8.5 W for 30 s). After HIFU treatment, the cells as well as untreated cells were then collected and lysed, which were then processed according to standard protocols of WB to evaluate the expression of CD44. For comparative analysis, β-actin was used as an internal control. Moreover, to observe whether CD44 facilitates the cellular uptake of PLip, 4T1 cells were seeded, cultured, and exposed to HIFU treatment as described above. Following HIFU irradiation, the medium was supplemented with 1 μg/mL of CD44 antibody before the addition of DiD-PLip (2 mg/mL). Following a 2 h incubation, cellular uptake was scrutinized using a confocal laser scanning microscope (Olympus, Tokyo, Japan) and flow cytometry (E_x/E_m = 640/670 nm; BD Biosciences, San Jose, CA, USA), and compared with the group that did not receive CD44 antibody treatment.

2.7. High ROS environment triggered by HIFU accelerated drug release

To assess the impact of ROS on drug release from PLip, 2 mL of PLip (2 mg/mL) was placed into a cellulose ester dialysis membrane (MW 8000−10,000 Da). Afterward, the bag was immersed in PBS containing 100 mmol/L hydrogen peroxide and 0.5% (*w*/*w*) Tween-80 or PBS containing 0.5% (*w*/*w*) Tween-80. The setup was agitated on a shaker at 37 °C and 100 rpm (TQ420, Hangzhou Aolaib Instrument Co., Ltd., China). At predetermined time points, 1 mL of the release medium was sampled and replaced with an equal volume of fresh release medium. The absorbance at 360 nm was measured using a UV−Vis spectrophotometer (Agilent, Santa Clara, CA, USA).

To verify that HIFU can create a high ROS environment both within tumor cells and in the surrounding environment, 4T1 cells were cultured in a 12-well plate overnight and received HIFU treatment (8.5 W for 30 s). Afterward, cells were immediately added with PLip (2 mg/mL) and incubated for 2 h. Additionally, separate control groups were included: a group treated solely with HIFU irradiation, a group treated solely with PLip, and a blank control group. The cells were then stained with ROSGreen™ H_2O_2 Probe for 30 min, and the intracellular hydrogen peroxide concentration was measured using a flow cytometer (E_x/E_m = 490/525 nm; BD Biosciences). The fluorescence of the supernatant, mixed in a 1:1 ratio with the probe working solution to a total volume of 100 μL, was measured by a microplate reader (E_x/E_m = 490/525 nm; Infinite® M200 PRO, Tecan, Zurich, Switzerland).

2.8. PLip and HIFU synergistically kill tumor cells in vitro

To explore the synergistic effect of PLip and HIFU treatment (HIFU + PLip) on killing tumor cells, 4T1 cells were seeded in a 12-well plate and cultured overnight. After trypsin digestion and collection, cells were treated with 8.5 W HIFU for 30 s. PLip and Lip were then added to the cell suspension to achieve a final concentration of 0.4 μg/mL of GA. After a further 24 h of culture, cell viability was assessed using the CCK-8 assay. Cells treated solely with HIFU, PLip, or Lip served as controls.

Additionally, to investigate the apoptotic-promoting effects of HIFU + PLip, 4T1 cells were cultured and treated as described above. 24 h later, cells were collected by centrifugation, followed by staining with Annexin V-FITC and PI in a dark environment at room temperature for 15 min. Subsequently, flow cytometric analysis was performed on the cells using FlowJo v.7.6.5 (Tree Star, Inc., Ashland, USA).

2.9. mRNA-seq of tumor cells after HIFU + PLip treatment

To observe the gene expressions of tumor cells after HIFU + PLip treatment, 4T1 cells were cultured in 6-well plates and incubated overnight. After trypsin digestion and collection, the cells were treated with 8.5 W HIFU for 30 s, followed by coincubation with PLip (2 mg/mL) for 12 h. Afterward, RNA was extracted from the cells using the Biozol RNA Miniprep Kit (BW-R7311, Peiwo, Beijing, China), following the manufacturer's protocol. RNA quality was assessed using Qubit 4.0 (Invitrogen, Carlsbad, CA, USA) and by electrophoresis on a denaturing agarose gel. RNA libraries were prepared using the VVAHTS® Universal V8 RNA-seq Library Prep Kit for Illumina (NR605-0, Vazyme, Nanjing, Jiangsu, China), followed by sequencing using the Illumina NovaSeq 6000 platform with the 150 paired-end sequencing strategy. Illumina adapter sequences were trimmed using Skewer (v 0.2.2). The quality checking was performed using FastQC (v 0.11.5). Then, clean reads were mapped to the human genome version hg38 using STAR (v 2.5.3a). StringTie (v 1.3.1c) was used to generate gene expression data, and differential gene expression was analyzed by the DESeq2 package (v 1.16.1). Pathway analysis was performed using the KEGG pathway database (https://www.genome.jp/kegg/pathway.html). A total of 1399 genes with a relevance score of 7 or higher with ROS were obtained through the GeneCards database (https://www.genecards.org), and these genes

were used in the subsequent analysis of significant differences related to ROS.

2.10. Pharmacokinetics and tissue distribution of PLip

To assess the pharmacokinetics and tissue distribution of PLip and the effect of HIFU on them, a breast cancer model was established in BALB/c mice by injecting 4T1 breast cancer cells into the right mammary gland. When the tumor reached a volume of approximately 300 mm^3, mice were randomly divided into four groups (HIFU + Lip, HIFU + PLip, Lip, and PLip), each consisting of three mice. For the HIFU + PLip or HIFU + Lip group, the tumor was irradiated with 8.5W HIFU for 30 s, and mice received an intravenous injection of 150 μL of DiD-PLip or DiD-Lip 2 h after HIFU treatment. For the PLip or Lip group, mice received only an injection of 150 μL of DiD-PLip or DiD-Lip. At various time points after injection, 20 μL of orbital blood was collected into heparinized tubes. The fluorescence intensity of these blood samples was quantitatively measured using a microplate reader (E_x/E_m = 640 nm/670 nm; Tecan). At 24 h after intravenous administration, mice were sacrificed, and major organs, including the tumor, were collected for *ex vivo* imaging using the IVIS Spectrum *in vivo* fluorescence imaging system (Rivvity, Woburn, MA, USA). After the imaging was completed, the organs and tumors were placed in PBS and homogenized using a tissue grinder (T10; Biheng Bio., Shanghai, China). The fluorescence intensity of these homogenates was subsequently measured using a microplate reader (E_x/E_m = 640 nm/670 nm; Tecan).

To monitor the accumulation of PLip in tumors at various time points, twelve tumor-bearing mice were subjected to the same experimental procedure as mentioned above, except for blood sampling. At specific time intervals, mice were subjected to the IVIS Spectrum *in vivo* fluorescence imaging system (Revvity, Waltham, MA, USA) to directly observe the accumulation of PLip at the tumor site.

To observe the distribution profile of PLip in tumor slices after HIFU treatment, twelve tumor-bearing mice were subjected to the same experimental procedure as mentioned above, except for blood sampling. 24 h later, tumors were excised for frozen sectioning, followed by CD44 antibody staining overnight at 4 °C. Subsequently, the sections were washed three times with 0.01 mol/L PBS for 5 min each and then incubated with Alexa Fluor® 568 Goat Anti-Rabbit IgG (1:400) at 37 °C for 30 min, followed by three washes with PBS. The sections were mounted using a mounting medium containing DAPI and observed under a fluorescence microscope (Eclipse Ci-L; Nikon, Tokyo, Japan). The entire process was conducted in a light-protected environment to prevent fluorescence quenching.

2.11. Anti-tumor efficacy of HIFU + PLip

To assess the anti-tumor efficacy of HIFU + PLip, six-week-old BALB/c mice underwent *in situ* mammary gland inoculation of 4T1 cells as described above. When the tumor volume reached approximately 100 mm^3, mice were randomly divided into six groups (HIFU + PLip, HIFU + Lip, HIFU, PLip, Lip, PBS), each consisting of six mice. Three of these groups received 8.5W HIFU for 30 s on the tumor and then an intravenous injection of 150 μL of PLip (28.89 μg of GA), Lip (28.89 μg of GA), or PBS 2 h after HIFU irradiation, respectively. The remaining three groups were administered only with PLip (28.89 μg of GA), Lip (28.89 μg of GA), or PBS without HIFU treatment. The same treatment was repeated 48 h later. Starting from the first treatment, the weight and tumor volume of the mice were recorded every two days. The tumor volume was calculated using Eq. (3):

$$\text{Tumor volume} = 0.5 \times \text{Length} \times \text{Width}^2 \quad (3)$$

On Day 15, when the tumor size in the PBS group reached 1500 mm^3, three mice from each group were randomly selected for routine blood and biochemical tests. Major organs were extracted for histopathological examination with hematoxylin and eosin (H&E) staining to verify the safety of the therapy. All mice were then sacrificed, and the tumors were photographed and weighed.

Considering that HIFU + PLip treatment could almost eliminate tumors when the tumor volume was small (100 mm^3), it was difficult to obtain tumor slices to observe the cell apoptosis in tumors after treatment. Thus, when their tumors reached 300 mm^3, the same cohort of tumor-bearing mice were randomly divided into six groups and received various treatments as described above to evaluate tumor apoptosis. On Day 7 after the first dosing, mice were sacrificed. Tumors were extracted, sectioned, and stained with Hematoxylin and Eosin (H&E) and Terminal deoxynucleotidyl transferase dUTP nick end labeling (TUNEL) following routine protocols. The H&E-stained slices were scanned using a slide viewer (VS200; Olympus, Tokyo, Japan), while the TUNEL-stained slices were examined using an automated acquisition system (TissueFAXS Plus; TissueGnostics GmbH, Vienna, Austria).

All experimental procedures were executed according to the protocols approved by Fudan University Animal Care and Use Committee.

2.12. PLip enhanced HIFU-induced ferroptosis within tumors

Similarly, to observe the ferroptosis in tumors after HIFU + PLip treatment, when the tumor volume reached approximately 300 mm^3, mice were randomly divided into four groups (HIFU + PLip, HIFU, PLip, PBS). Two of these groups received 8.5W HIFU for 30 s on the tumor and then an intravenous injection of 150 μL of PLip (28.89 μg of GA) or PBS 2 h after HIFU irradiation, respectively. The remaining two groups were administered only with PLip (28.89 μg of GA) or PBS without HIFU treatment. On Day 3, the tumors from each group were excised for frozen sectioning. These sections were stained with DCFH-DA for ROS detection and analyzed under a fluorescence microscope (Eclipse Ci-L; Nikon, Japan). The tumor samples were also tested for GSH concentration following the protocol of the GSH and GSSG Assay Kit. Similarly, on Day 7 post-treatment, the remaining mice had their tumors excised and sectioned for staining with C11 BODIPY 581/591 to monitor the LPO generation within the tumor.

All experimental procedures were executed according to the protocols approved by Fudan University Animal Care and Use Committee.

2.13. Data analysis

Data were presented as mean ± standard deviation (SD). Comparisons between the two groups were conducted using the *t*-test. Differences among multiple groups were determined using one-way ANOVA and two-way ANOVA. Bioinformatics analysis,

data interpretation, and graph visualization were performed using R v 3.6.3.

3. Results and discussion

3.1. Determination of the ferroptosis inducer

An initial analysis was conducted to compare the expression patterns of typical genes linked to ferroptosis in different subtypes of breast cancer and nearby normal tissues. As shown in Fig. 2A−E and Supporting Information Fig. S1, the expression levels of the 25 typical genes related to ferroptosis showed significant differences between tumor tissues and nearby normal tissues. Among them, ACLS4 (Fig. 2A), a prominent marker driving ferroptosis, was significantly downregulated in basal-like breast invasive cancers (BRCA-basal) compared with normal tissues, while the expression levels of AIFM2 (FSP1; Fig. 2B), SLC7A11 (Fig. 2C), and GPX4 (Fig. 2E), which are known to be essential suppressors of ferroptosis, exhibited a substantial reduction. Additionally, SLC40A1 (FPN1; Fig. 2D), an essential suppressor of ferroptosis, which functions as a transmembrane iron transporter, demonstrated a substantial upregulation in BRCA-basal compared with normal tissues. These data collectively indicate that basal-like breast cancer may be sensitive to ferroptosis-related drugs.

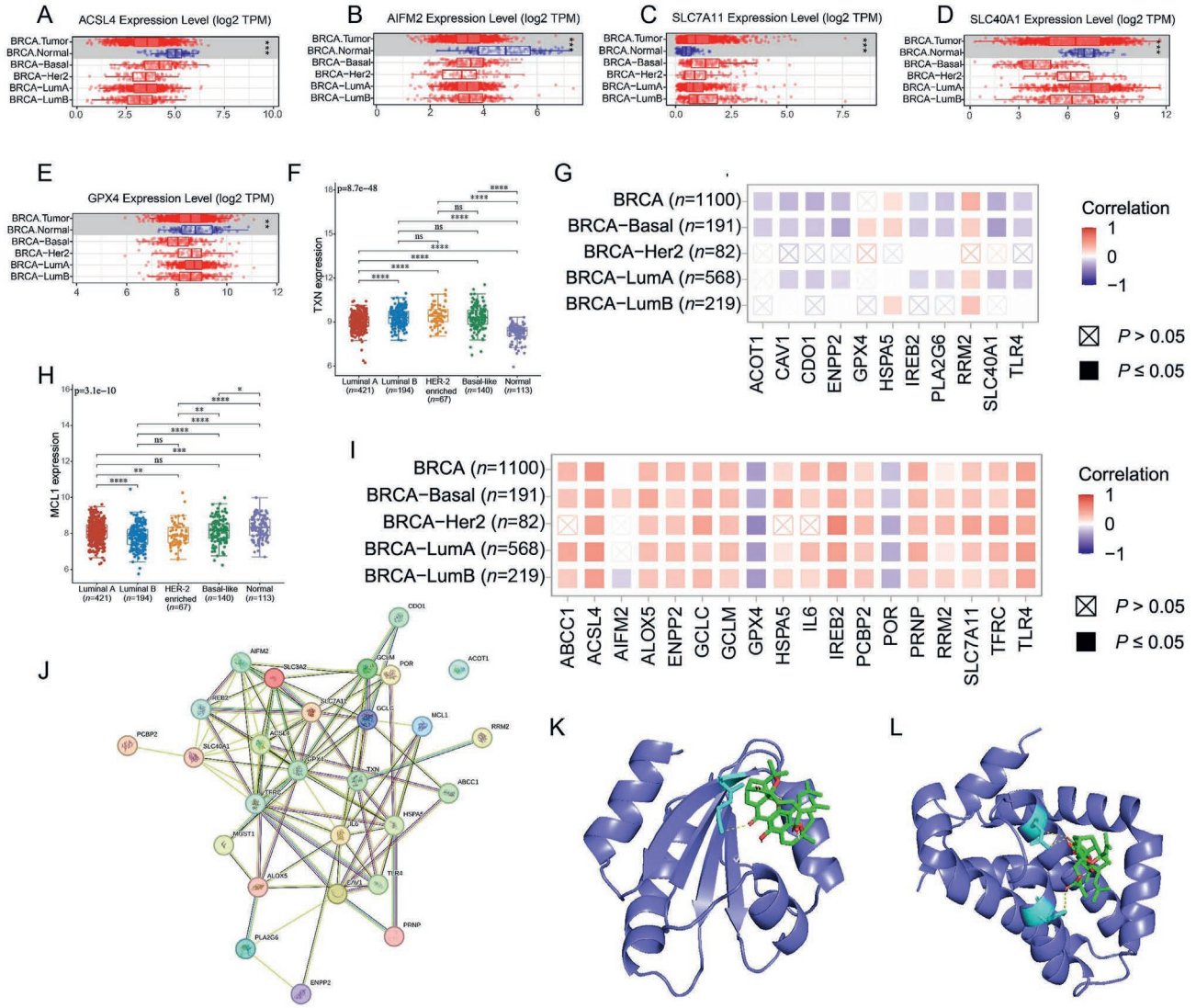

Figure 2 Expressions of ferroptosis-related genes in breast cancer subtypes and determination of the ferroptosis inducer. (A−E) The expression profiles of five representative ferroptosis-related genes, ACSL4 (A), AFIM2 (B), SLC7A11(C), SLC40A1 (D), and GPX4 (E), across distinct subtypes of breast cancers and in normal tissues. (F) Expression of the TXN gene in breast cancer subtypes and normal tissues. The statistical difference between two groups was compared through the Wilcox test, significance difference among three groups was tested with the Kruskal−Wallis test. (G) Ferroptosis-related genes correlated with the expression of TXN in breast cancer subtypes. (H) Expression of the MCL1 gene in breast cancer subtypes and normal tissues. (I) Ferroptosis-related genes correlated with the expression of MCL1 in breast cancer subtypes. (J) The protein-protein interaction networks diagram illustrates the interplay between TXN, MCL1, and 25 ferroptosis-related genes. (K, L) Molecular docking simulation illustrated the interactions of gambogic acid with TXN (K) and MCL1 (L) proteins. Green, gambogic acid; purple, protein; blue, amino acid residue. $*P < 0.05$, $**P < 0.01$, $***P < 0.001$, $****P < 0.0001$ *vs.* indicated; ns, no significance.

Considering the association between TXN[41], MCL-1[42], and oxidative stress, as well as the significant role of oxidative stress in ferroptosis[38,39], the gene expression of TXN and MCL-1 was investigated in several subtypes of breast cancer and normal tissues. The expression of TXN was upregulated in all subtypes of breast cancer, whereas the expression of MCL1 was reduced (Fig. 2F and H). These findings indicate that these proteins hold promise as prospective targets for therapeutic interventions. Additional analysis of the expression correlation between TXN, MCL1, and 25 ferroptosis-related genes revealed a significantly negative correlation between TXN and several ferroptosis-related genes (Fig. 2G). Out of all the subtypes, the basal subtype of breast cancers exhibited the highest connection with TXN, suggesting that this particular subtype is most suitable for regulating TXN and potentially leading to ferroptosis. Conversely, MCL-1 exhibited a significantly positive correlation with 15 genes related to ferroptosis (Fig. 2I). Additionally, protein-protein interaction (PPI) network generated for the aforementioned genes demonstrated that TXN and MCL-1 had a close relation with most of the ferroptosis-associated genes (Fig. 2J). As an inhibitor of both TXN and MCL1, GA could bind with TXN through one hydrogen bond with lysine (Lys) residues, and bind with MCL-1 through three hydrogen bonds with an arginine (Arg) residue and two histidine (His) residues (Fig. 2K and L), which suggest GA may induce ferroptosis in breast cancer.

Then, we tested the IC_{50} values of several potential ferroptosis inducers[37], including GA, against 4T1 cells in combination with HIFU (Supporting Information Table S1). It was found that GA, when combined with HIFU, demonstrated the best synergistic effect, resulting in the highest fold change in IC_{50} values. Specifically, the IC_{50} value of GA alone was 0.692 μg/mL, but when used in conjunction with HIFU, the IC_{50} value decreased by a factor of 4.380 to 0.158 μg/mL. Therefore, GA was utilized as a stimulator of ferroptosis in basal-like breast cancers, and the study will further highlight how HIFU drives GA-induced ferroptosis by influencing specific genes associated with tumor ferroptosis.

3.2. *Characterization of platelet-biomimetic liposomes*

The particle sizes of PLip, blank PLip, PLA, and Lip were measured using DLS. As shown in Fig. 3A, the average particle diameter of Lip was 115.7 ± 7.8 nm. The average size of PLip grew to 144.6 ± 1.9 nm due to the addition of the platelet membrane. Additionally, blank PLip had a somewhat smaller size, with an average diameter of 142.8 ± 0.9 nm. The zeta potential of the liposomes was determined by ELS. As presented in Fig. 3B, the mean potentials of PLip and Lip were −22.6 ± 1.1 mV and −26.4 ± 0.5 mV, respectively. The surface zeta potential was increased after the integration of the platelet membrane, possibly because of the presence of the neutral phospholipids phosphatidylcholine and sphingomyelin in the outer layer of the platelet membrane[48], or due to the shielding effect of membrane proteins on the negative charge of phosphate groups[49]. Cyro-EM imaging results demonstrated that PLip showed a consistent round shape with a uniform distribution and a particle diameter ranging from 140 to 160 nm (Fig. 3C and Supporting Information Fig. S2). To verify the successful fusion of platelet membranes with Lip, we conducted Western blot assays to detect the presence of key platelet membrane proteins, including CD41, CD62P, GPVI, and sodium-potassium ATPase in PLip. As illustrated in Supporting Information Fig. S3, the levels of these four membrane proteins in PLip were consistent with those in platelet membrane vesicles, indicating that the PLip successfully preserved the key proteins from the platelet membrane. These findings further validated the creation of platelet-biomimetic liposomes. Afterwards, the stability of PLip was investigated at a temperature of 4 °C. The particle diameter slightly increased to around 160 nm (Supporting Information Fig. S4A), while the polydispersity index showed a modest increase but stayed below 0.2 (Fig. S4B), indicating good stability *in vitro*. After a storage of seven days, there were no noticeable alterations in the visual characteristics of the PLip suspension. It still kept a light milky yellow without any signs of sedimentation or stratification.

3.3. *PLip and HIFU synergistically kill tumor cells in vitro*

We initially explored HIFU parameter optimization *in vitro*. As shown in the Supporting Information Fig. S5, as the duration of HIFU treatment increased, the viability of 4T1 cells decreased significantly. Especially after 50 s of treatment at the power of 8.5 W, the cell viability dropped sharply. By the 90-s mark, the cell viability was reduced to less than 5%, demonstrating that HIFU has a strong cytotoxic effect, with more prolonged exposure leading to a more pronounced decrease in cell viability. It was also found that cells were more likely to lose viability at higher power (10.1 W) ultrasound. HIFU irradiation at a power of 8.5 W for 30 s induced a mild reduction in cell viability, approximately 20%, and was therefore selected for this study. Then we investigated the cytotoxic effects of HIFU and different doses of GA on 4T1 cells. As shown in Supporting Information Fig. S6, the vitality of 4T1 cells rapidly declined as the concentration of GA increased. This suggests that 4T1 cells are highly sensitive to GA, with an IC_{50} value of 0.440 μg/mL. After subjecting 4T1 cells to 8.5 W HIFU for 30 s, the cell viability in the HIFU group dropped to 76.2 ± 3.7%. Interestingly, HIFU + PLip treatment exhibited the most pronounced inhibition of cell viability (Fig. 3D), with only 22.0 ± 4.2% cell viability, while PLip treatment and HIFU + Lip showed 78.8 ± 3.7% and 32.9 ± 2.3% cell viability, respectively. The combination index (CI) of PLip and HIFU, calculated using the Bliss combination index formula $\left(CI_{Bliss}(d_1,\ d_2) = \frac{E_{Bliss}(d_1,d_2)}{E(d_1,d_2)}\right)$[50,51], was 0.548, indicating that PLip and HIFU can synergistically kill tumor cells. The combination index of Lip and HIFU was 0.604, showing a lower synergistic effect than PLip and HIFU. To corroborate this finding, flow cytometric analysis was conducted using Annexin V-FITC/PI double staining to assess apoptosis. As shown in Fig. 3E and F and Supporting Information Fig. S7, the results revealed that the HIFU + PLip group had the highest percentage of total apoptotic cells (75.2%) and late apoptosis (67.1%) among all groups. All these results indicate that PLip can synergistically enhance HIFU's antitumor effect *in vitro*.

3.4. *HIFU enhanced the uptake of platelet-biomimetic liposomes by tumor cells in vitro*

Our studies revealed that the HIFU + PLip demonstrated a more potent cytotoxic effect on 4T1 cells compared to HIFU + Lip. To explore the underlying causes, a cellular uptake experiment was conducted. As presented in Fig. 3G and Supporting Information Fig. S8, PLip was more readily internalized by 4T1 cells compared with Lip, red blood cell-fused liposomes (RLip), and tumor cell membrane-fused liposomes (TLip). Flow cytometry

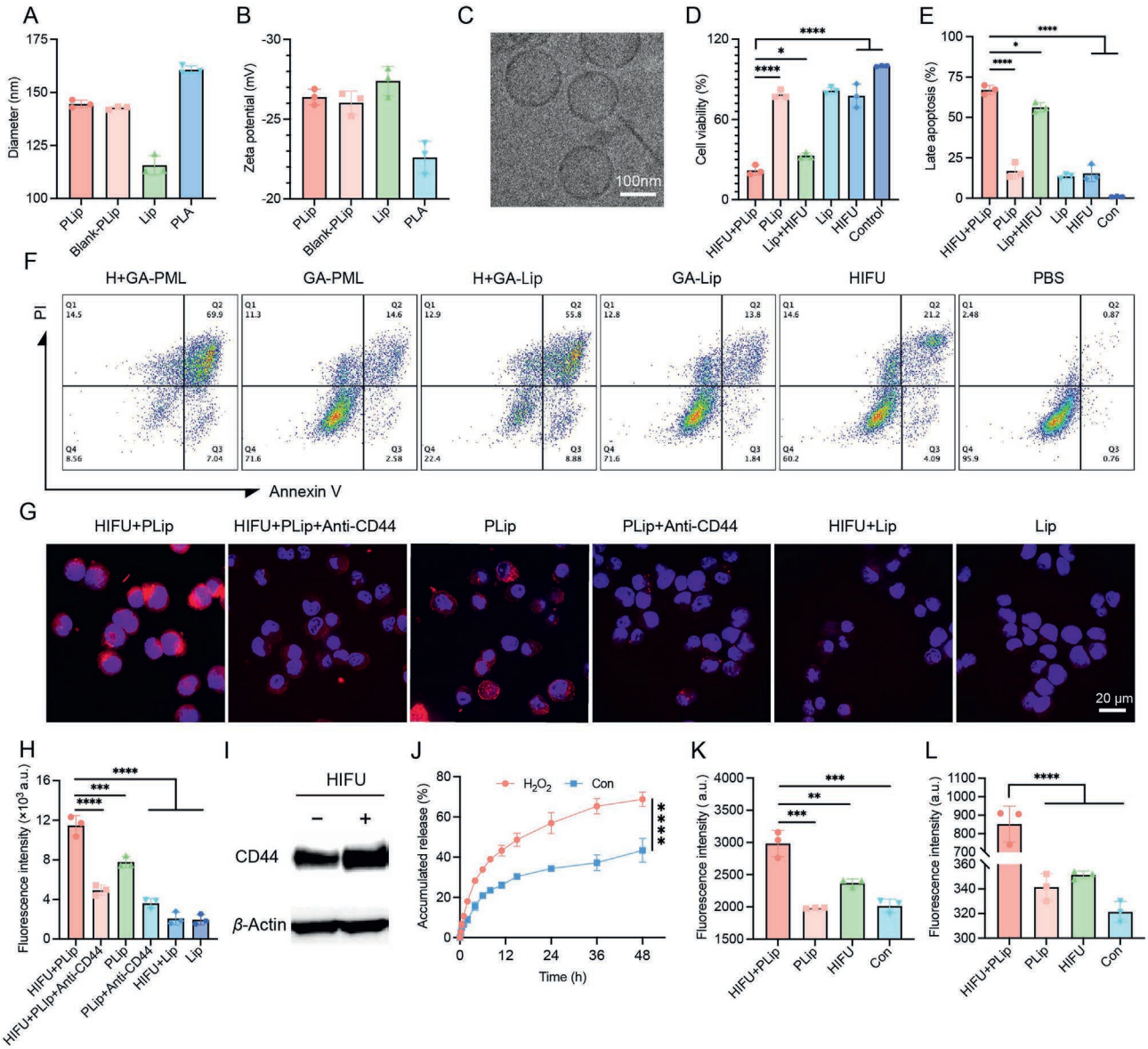

Figure 3 Characterization, cytotoxicity, uptake, and drug release of biomimetic liposomes. (A, B) Mean diameter (A) and Zeta potential (B) of PLip ($n = 3$). (C) The representative Cryo-EM image depicted PLip laden with gambogic acid. Scale bar = 100 nm. (D) CCK-8 assay to evaluate the viability of 4T1 cells after various treatments ($n = 3$). (E, F) Representative flow cytometry plots depicting apoptosis in tumor cells following various treatments (F), along with a corresponding statistical graph of late apoptosis (E) ($n = 3$). (G, H) Observations of cellular uptake of DiD-labeled liposomes under various treatments using fluorescence confocal microscopy (G, scale bar = 20 μm), and flow cytometric quantification (H) ($n = 3$). (I) Alterations of CD44 protein expression in tumor cells following HIFU treatment ($n = 3$). (J) Comparison of PLip's drug release profile in high H_2O_2 conditions versus an H_2O_2-free environment ($n = 3$). (K, L) Intracellular (K) and extracellular (L) H_2O_2 levels following various treatments ($n = 3$). Data are presented as mean ± SD. Statistical significance was analyzed by one-way ANOVA with a Tukey *post hoc* test. $^*P < 0.05$, $^{**}P < 0.01$, $^{***}P < 0.001$, $^{****}P < 0.0001$ *vs.* indicated; ns, no significance.

results demonstrated that the cellular uptake of PLip was 3.76 times higher than that of the Lip group (Fig. 3H). Furthermore, after HIFU irradiation, the uptake of PLip by 4T1 cells was significantly enhanced, suggesting that HIFU enhances the uptake of PLip. However, HIFU did not enhance the cellular uptake of Lip, RLip, and TLip. These findings indicate that when used in conjunction with HIFU, PLip demonstrates enhanced targeting specificity towards 4T1 tumor cells as compared to Lip, RLip, and TLip.

Delving deeper into the mechanism, we chose CD44, a protein that is commonly found in breast cancers[52] and serves as a major ligand for P-selectin on the surface of platelets[53]. It was notable that blocking CD44 on 4T1 cells with an antibody significantly reduced PLip uptake of 4T1 cells by 2.16-fold (Fig. 3G and H). Additionally, blocking CD44 also significantly reduced PLip uptake of HIFU-treated 4T1 cells by 2.32-fold. These results indicate that CD44 is involved in PLip uptake by 4T1 cells or HIFU-treated 4T1 cells. Thus, the expression levels of CD44 in 4T1 cells were assessed before and after HIFU treatment, revealing a notable rise post-HIFU treatment (Fig. 3I). This may be because HIFU induces localized heat and physical damage to tumor cells,

leading to immunogenic cell death (ICD), enhancing both innate and adaptive immune responses. The damage caused by HIFU activates various signaling pathways, including the NF-κB pathway and STAT3 pathway, which play a crucial role in cellular stress and inflammatory responses. By inducing the release of pro-inflammatory cytokines such as TNF-α, IL-6, and growth factors like EGF and PDGF, the activation of the NF-κB pathway[54,55] and STAT3[56] pathway can increase CD44 expression. Additionally, transcription factors such as AP-1 and HIF-1α, which respond to stress and hypoxia, can further regulate CD44 gene transcription. These findings suggest that HIFU boosts the active targeting capability of PLip rather than TLip and RLip towards 4T1 cells through upregulating CD44 expression on the cells.

3.5. High ROS environment triggered by HIFU accelerated drug release

Extensive research frequently centers on ROS-responsive drug delivery to obtain controlled drug release[57,58]. Additionally, several studies have demonstrated that HIFU can generate a high ROS concentration environment[33,59], which was validated by subsequent experiments. The primary structure of liposomes is the phospholipid bilayer, which contains unsaturated fatty acid chains that are susceptible to attack by ROS. Such attacks can induce lipid peroxidation, thereby compromising the integrity of the liposome and altering its membrane fluidity and permeability. This disruption can lead to the leakage of the liposome's contents or, in more severe cases, result in structural disintegration. In order to evaluate the ability of PLip to release the drug in response to ROS, *in vitro* release of PLip was conducted in a solution of PBS containing 100 mmol/L H_2O_2 and 1% Tween 80. It was shown that PLip showed a faster drug release in the ROS environment than in the normal environment (Fig. 3J). In addition, HIFU treatment induced a significant increase in H_2O_2 concentrations both intracellularly and extracellularly, with a 3-fold rise inside the cells and a 1.5-fold increase outside 2 h after treatment (Fig. 3K and L). The fast production of H_2O_2 indicates a prompt discharge of GA from PLip upon reaching the tumor site. To sum up, HIFU not only increased the internalization of PLip by tumor cells but also cooperatively generated a highly ROS environment, which promoted the release of PLip and hence the toxicity of PLip.

3.6. Validation of GA enhancing HIFU-induced ferroptosis in vitro

Previous research has verified that HIFU is capable of eliminating cancerous cells through thermal ablation. However, the mechanism by which PLip enhances cell death induced by HIFU, and whether PLip promotes ferroptosis caused by HIFU, remains unclear. To investigate this matter, three ferroptosis inhibitors, ferrostatin-1 (Fig. 4A), deferoxamine (Fig. 4B), and vitamin E (Fig. 4C), were employed to assess their impact on cell survival. Notably, three inhibitors all reduced cytotoxicity to different extents in the HIFU + PLip, HIFU, and PLip groups, indicating that the kind of cell death was linked to ferroptosis. In order to delve deeper into the molecular mechanism of ferroptosis, we initially examined the alterations in certain molecules that occur before the occurrence of ferroptosis. The level of intracellular GSH was seen to fall by half of the control level following HIFU + PLip therapy, while GSH levels in the PLip and HIFU groups decreased by 19.1% and 25.6%, respectively (Fig. 4D). Additionally, the levels of ROS in the HIFU + PLip group increased 2.64-fold compared to the control, as also visually confirmed by confocal imaging (Fig. 4E and F). In contrast, the PLip and HIFU groups only showed a 1.58- and 2.26-fold increase, respectively, which suggests that the combination of PLip and HIFU has a powerful potential to enhance the production of ROS. With regards to Fe^{2+} concentration in the HIFU + PLip group, a crucial ion influencing ferroptosis, there was a dramatic decrease to 12.5% of that in normal 4T1 cells (Fig. 4G and H), likely due to the intense ROS oxidizing Fe^{2+} to Fe^{3+}. Finally, the level of LPO, a key marker of ferroptosis, was found to be highest in the HIFU + PLip group, which was 1.50 times higher compared to that in the untreated group, as evidenced by confocal imaging and flow cytometry (Fig. 4I and J and Supporting Information Fig. S9). In contrast, the PLip group and the HIFU group showed only a slight increase in LPO levels. These findings collectively provide evidence that PLip enhances ferroptosis induced by HIFU.

3.7. Bioinformatics analysis of tumor cells after HIFU + PLip treatment

The preliminary findings suggest that PLip can augment the ferroptotic cytotoxic effects of HIFU at the cellular level. To elucidate the specific mechanisms by which PLip enhances HIFU's lethality towards tumor cells, we proceeded with transcriptomic sequencing of tumor cells treated differently, analyzing changes at the genetic expression level. The Gene Set Enrichment Analysis (GSEA) for ferroptosis-related genes (Fig. 5A and B, Supporting Information Fig. S10A−S10C) revealed an enrichment score of 0.63 in the HIFU + PLip group compared to the HIFU group (Fig. 5A), indicating PLip's potential to intensify the ferroptotic effect induced by HIFU. In contrast, the HIFU versus control group comparison yielded an enrichment score of only 0.30. The hits plot marked the position of each ferroptosis gene within the complete gene ranking list, where the left-sided 'leading edge subset' contributed predominantly to the enrichment score and constituted the core gene set. It was evident that HIFU + PLip treatment significantly upregulated eleven ferroptosis-associated genes compared to both HIFU treatment and control, with respective tags% of 35% and 34%. Subsequent volcano plots (Fig. 5C and D, Fig. S10D−S10F) depicted the overall differential gene expression, with upregulated genes in red, downregulated in blue, and nonsignificant changes in gray, pinpointing the location of significant ferroptosis genes within these plots. Specifically, in the comparison of HIFU + PLip with control (Fig. 5C), the expression of ferroptosis-associated genes, including FTH1, SESN2, IL1B, IL6, HSPB1, ENPP2, HMOX1, FTL1, CHAC1, SQSTM1, SLC7A11, and MGST1, were notably upregulated. In comparison with the HIFU group, ferroptosis-associated genes like GCLM, FTH1, IL6, ENPP2, SLC3A2, and SESN2 demonstrated significant upregulation in the HIFU + PLip group (Fig. 5D). The substantial enhancement of ferroptotic effects by HIFU in the presence of PLip was thereby highlighted. The heatmap in Fig. 5E visually illustrates the expression differences of ferroptosis pathway genes and related pathways across the HIFU + PLip, HIFU, Lip, and control groups, revealing an upregulation of seven genes associated with mineral absorption and six with the glutathione metabolism pathway. The KEGG pathway enrichment analysis revealed that, relative to HIFU treatment, HIFU + PLip treatment significantly enriched differential genes in pathways related to ferroptosis, fluid shear stress, glutathione metabolism, the TNF signaling pathway, and the IL-17

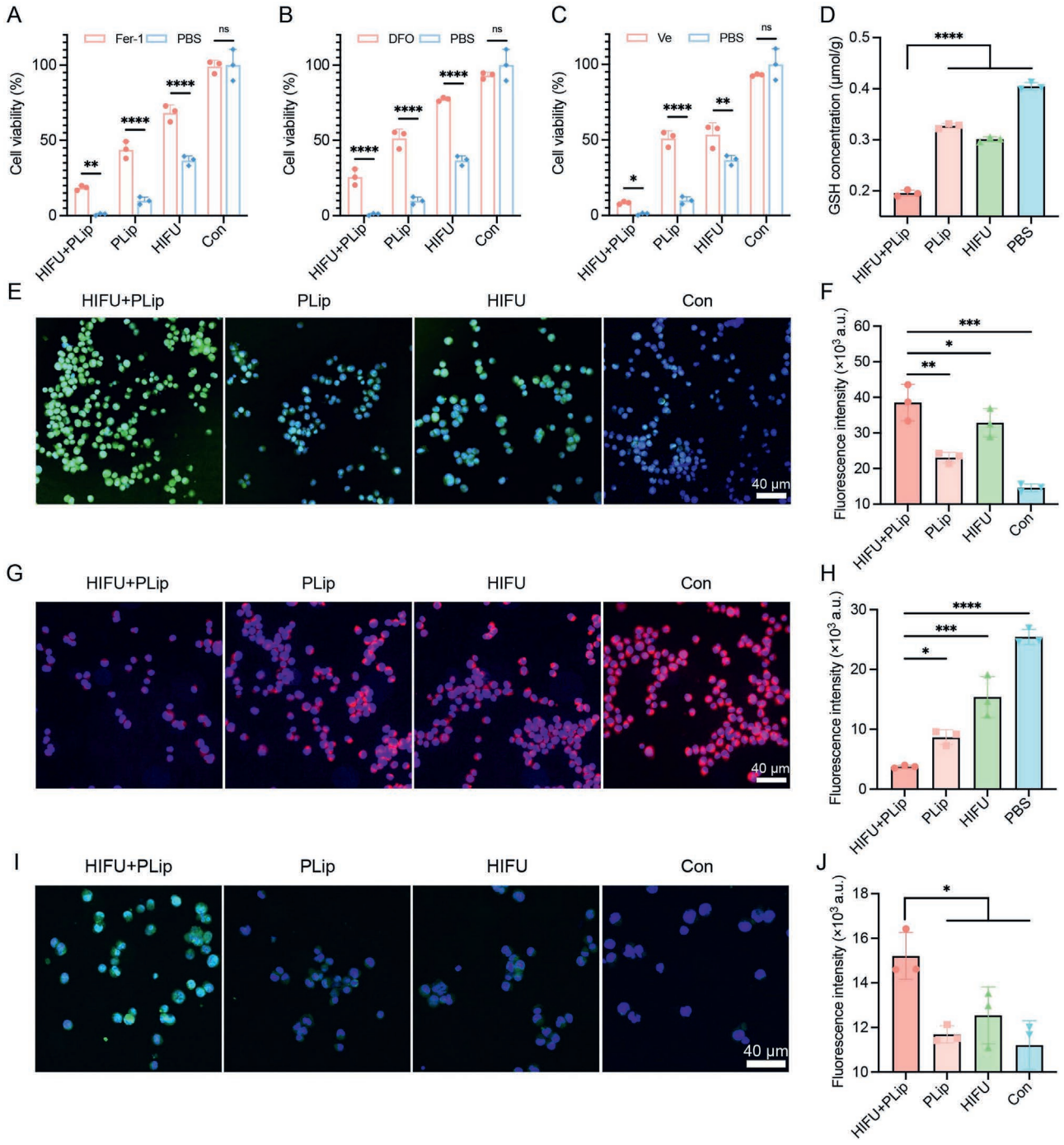

Figure 4 Validation of GA enhancing HIFU-induced ferroptosis *in vitro*. (A–C) The impact of three ferroptosis inhibitors, Fer-1 (A), DFO (B), and Ve (C), on tumor cell viability under different treatments ($n = 3$). (D) The GSH levels in 4T1 cells after various treatments ($n = 3$). (E, F) Flow cytometry quantification (F) and confocal microscopy visualization (E, scale bar = 40 μm) of ROS levels in 4T1 cells after different treatments using DCFH-DA staining ($n = 3$). (G, H) Assessment of intracellular divalent iron ion concentration following various treatments with the FerroGreen probe, demonstrated through confocal imaging (G, scale bar = 40 μm) and flow cytometry quantification (H) ($n = 3$). (I, J) Confocal microscopy (I, scale bar = 40 μm) and flow cytometry (J) assessments of lipid peroxidation on the membrane of 4T1 cells after various treatments using the C11-BODIPY probe ($n = 3$). Data are presented as mean ± SD. Statistical significance was analyzed by one-way ANOVA with a Tukey *post hoc* test. *$P < 0.05$, **$P < 0.01$, ***$P < 0.001$, ****$P < 0.0001$ *vs.* indicated; ns, no significance.

signaling pathway (Fig. 5F, Fig. S10G–S10I). The introduction of PLip to HIFU-treated tumor cells markedly increased the expression of specific ferroptosis genes, such as HSPB1, HMOX1, and SLC7A11, by 2.3, 3.1, and 4.11-fold, respectively (Fig. 5G). The FPKM values for the TXN1, TXN2, and MCL1 genes in 4T1 cells were lower after HIFU + PLip treatment compared to PLip treatment (Supporting Information Fig. S11). This indicates a reduction in the expression levels of these genes, suggesting that

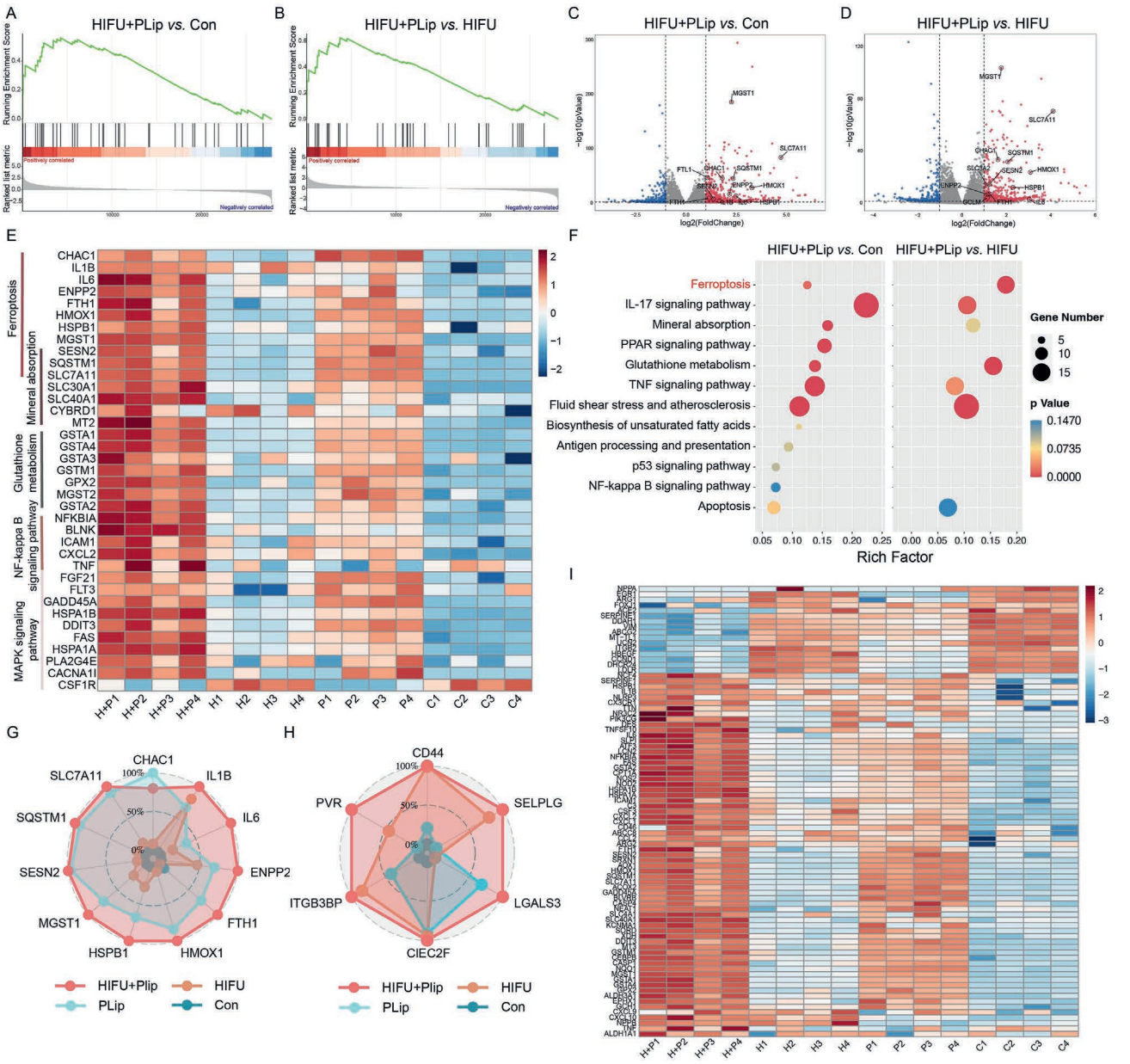

Figure 5 Bioinformatics analysis of mRNA expressions in tumor cells after HIFU + PLip treatment. (A, B) Gene Set Enrichment Analysis (GSEA) of the ferroptosis gene set (n = 4); (A) HIFU + PLip *vs.* Con and (B) HIFU + PLip *vs.* HIFU. (C, D) Volcano plot illustrating upregulated and downregulated genes in cells subjected to different treatments (n = 4); (C) HIFU + PLip *vs.* Con and (D) HIFU + PLip *vs.* HIFU. (E) Heatmap depicting the typical differentially transcribed RNA in 4T1 cells following various treatments (n = 4). (F) Enrichment analysis of KEGG pathways related to ferroptosis in differentially expressed genes within 4T1 cells (n = 4). (G) Radar chart displaying normalized FPKM values of ferroptosis-related genes after different treatments (n = 4). (H) Circular heatmap depicting the expressions of receptor genes potentially associated with PLip targeting after different treatments (n = 4). (I) Heatmap illustrating differentially expressed genes related to ROS generation after different treatments (n = 4). C1-4, H1-4, P1-4, H + P1-4 indicated control, HIFU, PLip, and HIFU + PLip treatment, respectively.

HIFU treatment augments the inhibitory effect of PLip on their expression. These outcomes suggest that PLip not only promoted HIFU-induced ferroptosis but also activated an immune response.

In our previous experiments, it was shown that HIFU treatment could upregulate CD44 expression on tumor cells, and blocking the CD44 receptor could inhibit PLip uptake by HIFU-treated tumor cells. To explore whether other receptors on tumor cells are involved in PLip uptake, we identified the expression of several possible genes associated with PLip targeting to tumor cells. As presented in Fig. 5H, on the mRNA level, the expression of CD44 was significantly elevated after HIFU or HIFU + PLip treatment, along with other genes such as SELPLG—another ligand for P-selectin[60,61], LGALS3—whose galectin-3 expression binds with GPVI on platelet surfaces[62], CLEC-2—the sole receptor for Podoplanin on platelets[63], integrin beta 3 binding protein (ITGB3BP), and PVR—a ligand for CD226 on platelets[64], all of

which were significantly upregulated. These findings suggest that in addition to CD44, other receptors on tumor cells may contribute to the enhanced targeting capability of PLip after HIFU treatment.

Recent investigations have verified that HIFU has the ability to substantially strengthen the oxidative stress conditions within tumors. In order to investigate the impact of HIFU and PLip on oxidative stress at the transcriptional level, we extracted the relevant gene data from the GeneCards database (https://www.genecards.org). Specifically, we focused on 1399 genes with a score of 7 or higher. By analyzing the heat map in Fig. 5I, we were able to accurately identify significant changes in the expressions of 83 genes related to oxidative stress following various treatments, showing an enhanced ROS environment after HIFU + PLip treatment. For instance, the expressions of genes like NOS2, which has a direct role in the creation of nitric oxide (NO), and HMOX1, responsible for the generation of carbon monoxide, were significantly increased after HIFU + PLip treatment.

3.8. *HIFU enhanced the tumor-targeting ability of PLip*

We first examined the pharmacokinetics of PLip *in vivo*. As shown in Fig. 6A and Supporting Information Table S2, the half-life of

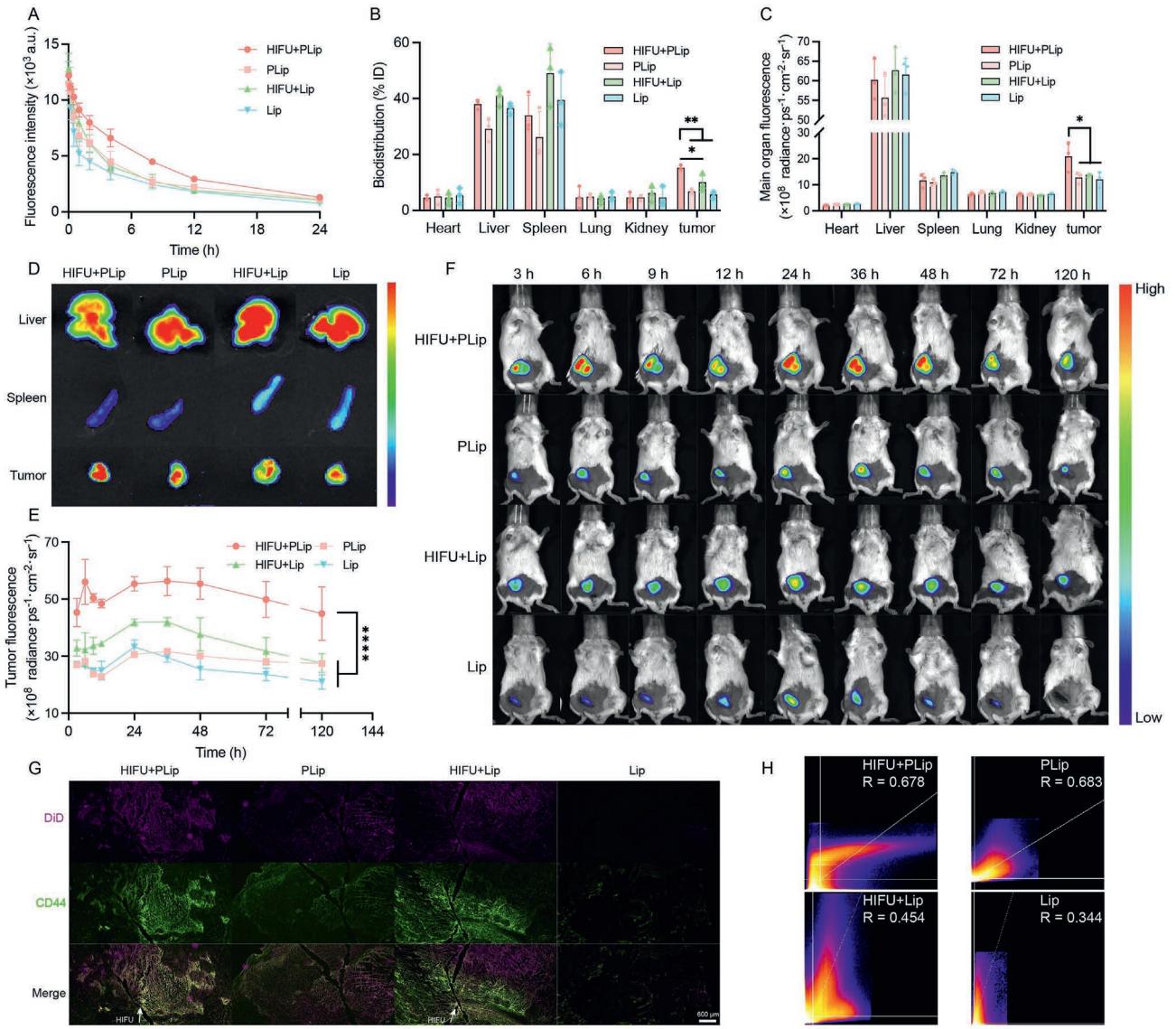

Figure 6 Enhanced active targeting of PLip to tumors after HIFU treatment. (A) 2 h after HIFU treatment, the fluorescence intensity in the blood of mice was measured at varying time points following the injection of different DiD-labeled liposomes. ($n = 3$). (B) 24 h post-injection, fluorescence intensity was collated from homogenates of major organs and tumors and expressed as % ID (percentage of injected dose) ($n = 3$). (C, D) 24 h post-injection, fluorescence imaging of excised organs and tumors (D) was performed, followed by semi-quantitative analysis (C). (E, F) Following various treatments, semi-quantitative results (E) and representative *in vivo* fluorescence images (F) were obtained from 4T1 tumor-bearing mice at various time points ($n = 3$). (G, H) 24 h following injection, representative immunofluorescence images of tumor sections (G) revealed the accumulation and targeting pattern of PLip within the tumors, accompanied by a co-localization analysis (H) of the fluorescence signals. Purple, PLip or Lip; green, CD44. Scale bar = 600 μm. Data are presented as mean ± SD. Statistical significance was analyzed by one-way ANOVA with a Tukey *post hoc* test. $^{*}P < 0.05$, $^{**}P < 0.01$, $^{****}P < 0.0001$ *vs.* indicated.

liposomes in the whole blood for the HIFU + PLip group was 7.49 h, while that for the PLip group was 7.11 h. However, HIFU treatment extended the circulation of PLip without statistical significance. The potential mechanisms by which HIFU prolongs the circulation of PLip could involve the immune cell hijacking. HIFU disrupts tumor tissue, thereby activating the immune system and leading to enhanced recognition and uptake or binding of liposomes by the circulating immune cells, such as neutrophils and monocytes. By hijacking these immune cells, PLip circulates longer in the whole blood. Additionally, we employed UPLC-MS to determine the pharmacokinetics of gambogic acid in the plasma (Supporting Information Fig. S12 and Table S3). It was revealed that in the PLip group, the half-life of GA was 5.11 h. Upon introducing HIFU treatment, the half-life decreased to 4.15 h. In comparison, the Lip group exhibited a shorter half-life of only 3.90 h. Additionally, PLip significantly increased the area under the curve (AUC) of gambogic acid in the plasma compared with Lip, indicating improved circulation time and drug exposure, which may enhance therapeutic efficacy and reduce dosing frequency. However, after HIFU treatment, the AUC of both PLip and Lip groups decreased. Interestingly, the half-life of fluorescence-labeled PLip was longer compared to GA. This may be because we measured the concentration of GA in the plasma, while the fluorescence-labeled PLip was detected in the whole blood. Over time, liposomes can be progressively taken up by circulating blood cells, which could contribute to a longer detectable presence of the fluorescence-labeled PLip in the circulation.

24 h after injecting DiD-labeled liposomes into mice bearing 4T1 tumors, the animals were sacrificed, and their major organs and tumors were harvested to prepare tissue homogenates for quantitative fluorescence analysis. It was observed that in the HIFU + PLip group, nanoparticle accumulation in tumors was 1.5 times and 2.3 times higher compared to that in the HIFU + Lip and PLip, respectively (Fig. 6B). Additionally, the HIFU + Lip group also showed a notable increase of nanoparticle accumulation in tumors compared to the HIFU group, potentially benefiting from the enhanced permeability of the blood-tumor barrier after HIFU treatment[31,65]. Notably, the PLip group, compared to the Lip group, demonstrated lower accumulation in the liver and kidneys. This reduction was attributed to the immune-compatibility of platelet-biomimetic liposomes and the diminishment of macrophage uptake[43]. Intriguingly, liver and spleen uptake of liposomes increased following HIFU irradiation, possibly

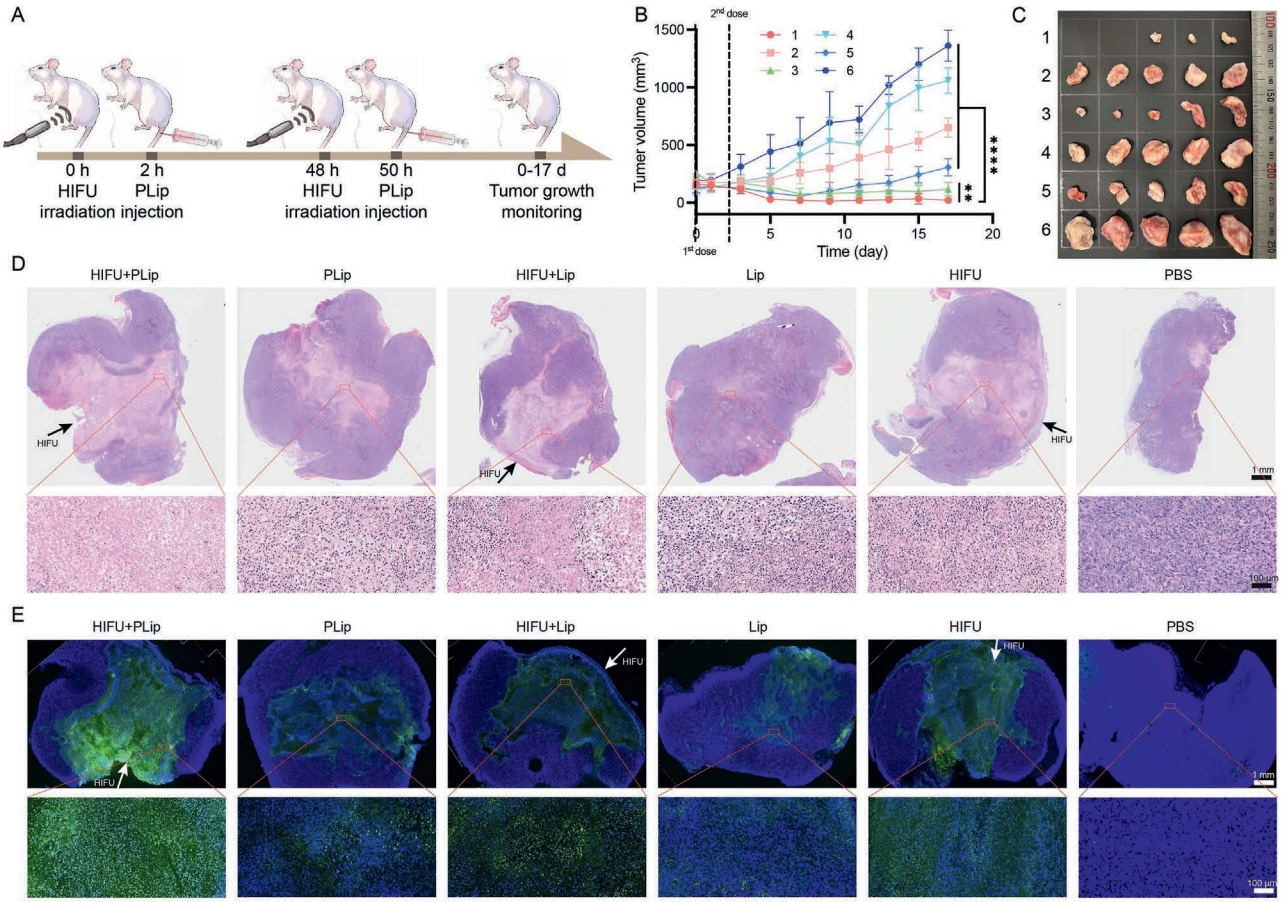

Figure 7 PLip enhanced the anti-tumor efficacy of HIFU *in vivo*. (A) Schematic diagram of cancer treatment strategies. (B) Changes in tumor volume within 15 days following various treatments ($n = 5$). 1, HIFU + PLip; 2, PLip; 3, HIFU + Lip; 4, Lip; 5, HIFU; 6, PBS. (C) Image of tumors on day 15 after various treatments ($n = 5$). 1, HIFU + PLip; 2, PLip; 3, HIFU + Lip; 4, Lip; 5, HIFU; 6, PBS. (D, E) Representative H&E-stained tumor sections (D) and TUNEL-stained sections (E) along with their magnified microscopic images. White arrows indicated the HIFU direction. Scale bars: overview images = 1 mm; magnified images = 100 μm. Data are presented as mean ± SD. Statistical significance was analyzed by one-way ANOVA with a Tukey *post hoc* test. $^{**}P < 0.01$, $^{****}P < 0.0001$ *vs.* indicated.

due to HIFU-induced macrophage activation[66] and a systemic immune response[67,68]. *Ex vivo* fluorescence imaging of the major organs and tumors revealed similar patterns of high tumor accumulation and liver and spleen distribution (Fig. 6C and D). To monitor the accumulation of liposomes within tumors over time, mice bearing 4T1 tumors were injected with an equal dose of DiD-labeled liposomes. Live fluorescence imaging was performed at specific time points, and the average fluorescence intensity of the tumor was obtained (Fig. 6E and F). It was found that the AUC of the tumor fluorescence intensity-time curve for the HIFU + PLip treatment group was 1.5 times that for the HIFU + Lip group and 1.7 times that for the PLip group, indicating HIFU enhanced efficient accumulation of PLip within the tumor. It was notable that at 6 h after injection, the tumor fluorescence signals in the HIFU + PLip group reached a local peak. This peak could be attributed to the reversible nature of focused ultrasound's barrier-opening effect[69], where a subsequent decrease in the permeability led to a reduction in tumor accumulation of nanoparticles.

We also evaluated the tumor targeting ability of PLip compared to RLip and TLip by fluorescence imaging. As shown in Supporting Information Fig. S13A−S13C, HIFU treatment significantly enhanced the accumulation of PLip in tumors, with the fluorescence intensity of tumors significantly higher than that of other groups at each time point after intravenous injection. However, HIFU treatment did not significantly enhance the accumulation of TLip in tumors. The AUC of the HIFU-PLip, PLip, HIFU-TLip, TLip, and HIFU-RLip groups were 5.90, 3.26, 2.43, 2.41, and 1.35 folds that of RLip, respectively. These results suggest that, with the assistance of HIFU, PLip exhibits superior *in vivo* tumor-targeting capabilities compared to RLip and TLip. As shown in Fig. S13D, *ex vivo* imaging showed results similar to those obtained from *in vivo* imaging. It was observed that the tumor accumulation of liposomes in the HIFU-PLip group was higher than in any other group. All these results suggest that HIFU can effectively enhance the tumor-targeting capabilities of PLip, while its effect on RLip and TLip remains minimal.

To further investigate other factor changes induced by HIFU that enhance tumor accumulation, we selected CD44, a protein capable of binding to the P-selectin on the platelet membrane, as the target protein. 24 h after administering DiD-labeled liposomes, tumors were excised for immunofluorescence staining of CD44 protein. As observed in Fig. 6G, there was a notable increase in CD44 expression, with DiD-labeled PLip colocalized with CD44 both in the presence and absence of HIFU treatment. However, this phenomenon was not observed in the HIFU + Lip or Lip group. Finally, the colocalization of CD44 and liposomes was assessed, revealing that the majority of the scatter plots (Fig. 6H) for the PLip group and HIFU + PLip group were aligned along the diagonal, with a colocalization coefficient of approximately 0.68, while the Lip group had a colocalization coefficient of only around 0.34. These results suggest that PLip can target the tumor cell *via* CD44.

3.9. PLip enhanced the efficacy of HIFU in the treatment of tumors

The treatment regimen shown in Fig. 7A was used to investigate the antitumor efficacy of HIFU + PLip on the 4T1-bearing mouse model. Following various treatments, the volume of the tumor was

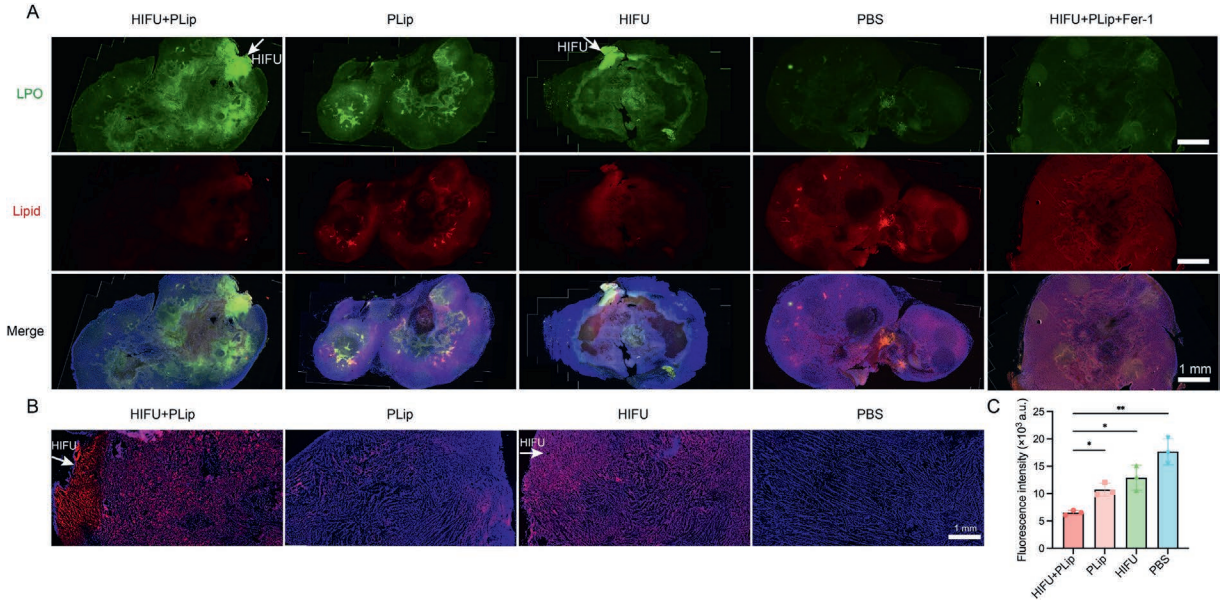

Figure 8 Validation of GA enhancing HIFU-induced ferroptosis *in vivo*. (A) Representative immunofluorescence images of tumor sections stained with C11-BODIPY following various treatments. Blue: nuclei; green: LPO; red: normal lipids. White arrows indicated the HIFU direction. Scale bar = 1 mm. (B) Representative immunofluorescence images of tumor sections stained with DCFH-DA after various treatments. Blue: nuclei; red: ROS. Scale bar = 1 mm. (C) Assessment of intracellular divalent iron ion concentration in tumors following various treatments with the FerroGreen probe ($n = 3$). Data are presented as mean ± SD. Statistical significance was analyzed by one-way ANOVA with a Tukey *post hoc* test. $^{*}P < 0.05$, $^{**}P < 0.01$ *vs.* indicated.

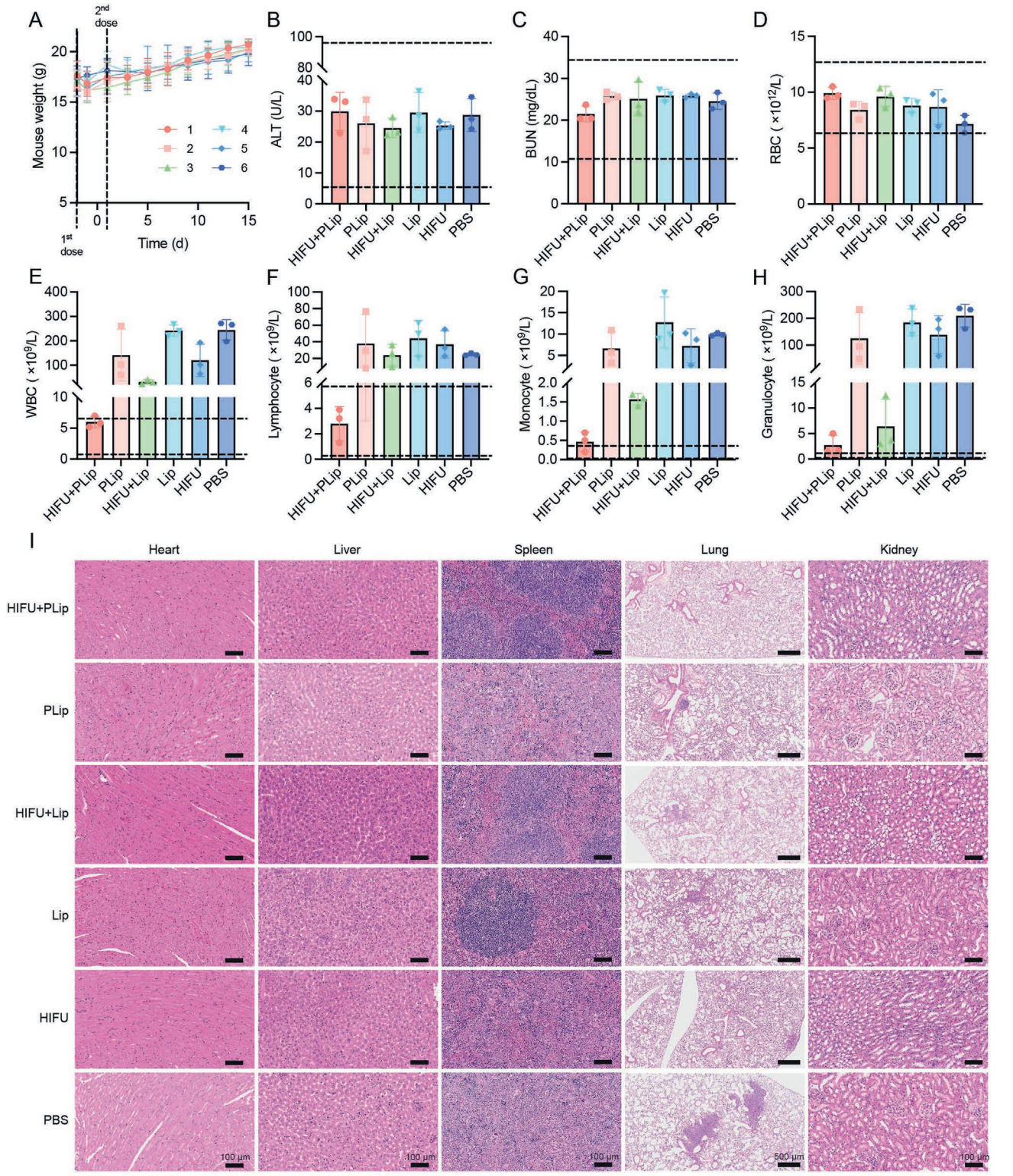

Figure 9 Biocompatibility of HIFU + PLip treatment. (A) Weight changes in mice post two treatment sessions after various treatments. The groups were categorized as follows: 1, HIFU + PLip; 2, PLip; 3, HIFU + Lip; 4, Lip; 5, HIFU; 6, PBS ($n = 5$). (B, C) Liver and kidney function indicators ALT (B) and BUN (C) in biochemical blood tests after various treatments. The black dashed line represented the reference range for normal BALB/c mice ($n = 3$). (D−H) Blood routine test assessed various blood cell counts, including red blood cells (D), white blood cells (E), lymphocytes (F), monocytes (G), and granulocytes (H). The black dashed line represented the reference range for normal BALB/c mice ($n = 3$). (I) Representative micrographs of H&E-stained sections of the major organs of the mouse after various treatments. Scale bar = 100 μm. Data are presented as mean ± SD.

consistently documented (Fig. 7B). Once the tumor volume surpassed 1500 mm^3, all of the mice were euthanized in order to capture images of the tumor (Fig. 7C) and measure their weight (Supporting Information Fig. S14). The tumor volume in the HIFU group initially fell by 56.9% in the first week, indicating effective tumor destruction. However, the tumor volume then grew fast, possibly because HIFU was unable to properly irradiate all tumors, resulting in tumor recurrence. The tumor inhibition rate of the PLip group was 68.3%, which was higher than the rate of the Lip group (47.7%), indicating that PLip has a stronger anti-tumor effect than Lip. This may be due to the enhanced active targeting ability of PLip, which is provided by the platelet membrane. When compared to other treatments, HIFU + PLip treatment sharply suppressed tumor growth, significantly decreased tumor weight by 97.5%, and eliminated the tumors in two animals. These findings suggest that PLip can efficiently collaborate with HIFU to inhibit the recurrence of tumors. H&E and TUNEL staining were conducted to assess the extent of damage to tumor tissues resulting from various treatments. In the three groups that received HIFU treatment, the nuclei aligned with the direction of HIFU-irradiation were significantly disturbed (Fig. 7D). PLip or Lip treatment resulted in minimal damage to the tumor, while the combination of PLip and HIFU treatment caused the most significant damage to the tumor, characterized by a most extensive nuclear fragmentation and pyknosis among all groups. In agreement with the H&E staining results, TUNEL staining results revealed that the HIFU + PLip group exhibited the most prominent and widespread apoptotic signals among all groups (Fig. 7E and Supporting Information Fig. S15). The results suggest that PLip improves the anti-tumor efficacy of HIFU.

3.10. Validation of GA enhancing HIFU-induced ferroptosis in vivo

Additional examination of the processes that combat tumors uncovered the potential of HIFU + PLip for triggering ferroptosis. On Day 7 after the first treatment, the tumors were extracted, sliced, and stained with LPO probe (Fig. 8A, Supporting Information Fig. S16A). The HIFU group exhibited obvious LPO fluorescence signals along the direction of HIFU treatment, while PLip exhibited low LPO fluorescence signals with an uneven distribution pattern, probably due to the limited penetration ability of PLip inside the tumor. Compared with HIFU or PLip treatment, HIFU + PLip treatment showed much stronger LPO signals along with the direction of HIFU treatment, with almost no normal lipids observed. Importantly, administering the ferroptosis inhibitor Fer-1 led to a significant reduction in LPO fluorescence in tumors treated with HIFU + PLip. On Day 5 after the first treatment, the tumors were extracted, sliced, and stained with the DCFH-DA probe for ROS detection (Fig. 8B, Fig. S16B). It was found that HIFU treatment induced extensive ROS generation in tumors along with the HIFU direction, while PLip caused weak ROS production inside tumors. Compared with HIFU or PLip treatment, HIFU + PLip treatment showed much stronger ROS signals along with the HIFU direction. Additionally, the GSH concentration in tumors of the HIFU + PLip group was approximately halved compared to that of the HIFU or PLip group and only 29.1% of that of the control group (Supporting Information Fig. S17). Moreover, intracellular Fe^{2+} levels in tumors were approximately halved after HIFU + PLip treatment compared to HIFU treatment alone (Fig. 8C). The observed alterations in multiple ferroptosis-related parameters indicate that PLip amplifies the occurrence of HIFU-induced ferroptosis in cancerous cells.

3.11. Biocompatibility of HIFU + PLip

To ascertain the safety of this therapy, we monitored the mice's weight every other day for two weeks post-treatment. Observations shown in Fig. 9A indicated a gradual increase in their weight. On the Day 15 post-treatment, further monitoring of the mice's complete blood count and biochemical markers, including a series of liver and kidney function indicators, AST (Fig. 9B), BUN (Fig. 9C) and others (Supporting Information Fig. S18A−S18D), revealed values within the normal range after various treatments. These findings substantiated that HIFU + PLip treatment did not cause significant damage to liver or kidney functions. Hematological assessments (Fig. 9D, and Fig. S18E−S18H) revealed that PLip did not induce serious toxicological issues such as hemolysis, and platelet counts (Fig. S18D) also remained within the normal range. Upon counting immune-related cells, it was observed that the white blood cells (Fig. 9E), lymphocytes (Fig. 9F), monocytes (Fig. 9G), and granulocytes (Fig. 9H) in the HIFU + PLip experimental group were all within or close to the normal range. This might be attributed to the near eradication of the tumor in the HIFU + PLip group on Day 15. Post-treatment, major organs of the mice were eviscerated for H&E staining (Fig. 9I). The images revealed no significant pathological changes in the heart, liver, spleen, and kidneys across all groups. Notably, in the HIFU + PLip group, no metastasis nodules were observed in the lungs, while the other five groups exhibited varying degrees of tumor metastasis in the lungs, which indicates that HIFU + PLip therapy effectively inhibits tumor metastasis. These results suggest that HIFU + PLip exhibits favorable biological safety.

4. Conclusions

This study employed HIFU to create a tumor microenvironment characterized by elevated levels of ROS and CD44. This milieu has a high capability to attract platelet-like liposomes loaded with gambogic acid and facilitate their effective release, potentially enhancing targeted tumor drug delivery and antitumor efficacy of drugs. Additionally, we found that PLip had the ability to intensify the ferroptosis effect generated by HIFU, leading to improved efficacy in treating tumors. This study presents an approach that offers a theoretical foundation for using medical devices such as HIFU to deliver nanomedicines to tumors more efficiently. It also highlights the potential of physical treatment methods to directly modify the tumor microenvironment, which in turn affects the behavior of nanomedicines in the body. In general, this study presents new strategies for leveraging the synergistic effect of nanomedicines and medical devices to maximize the anti-tumor efficacy.

Acknowledgments

The work was supported by National Key Research and Development Program, China (2024YFA0919100), National Natural Science Foundation of China (82230067, 82071915, 81773283).

Author contributions

Ruizhe Xu completed all the experiments, data analysis, and paper writing. Ying He, Xuejing Li, Xiaomin Su, Xifeng Qin, Ying He,

Siyu Wang, Yue Liu, Jiayi Wu, Ting Wang, Mingyang Liu, Boshu Ouyang prepared the experimental materials and assisted in some experiments. Jia Li and Wuli Yang provided a review of the article. Bo Zhang and Zhiqing Pang reviewed the experimental data, supervised and led the experiment, revised the article, and provided financial support.

Conflicts of interest

The authors declare no conflicts of interest.

Appendix A. Supporting information

Supporting Information to this article can be found online at https://doi.org/10.1016/j.apsb.2026.02.024.

References

1. Rosenblum D, Joshi N, Tao W, Karp JM, Peer D. Progress and challenges towards targeted delivery of cancer therapeutics. *Nat Commun* 2018;**9**:1410.
2. Phung CD, Nguyen BL, Jeong JH, Chang JH, Jin SG, Choi HG, et al. Shaping the "hot" immunogenic tumor microenvironment by nanoparticles co-delivering oncolytic peptide and TGF-β1 siRNA for boosting checkpoint blockade therapy. *Bioeng Transl Med* 2023;**8**: e10392.
3. Fan D, Cao Y, Cao M, Wang Y, Cao Y, Gong T. Nanomedicine in cancer therapy. *Signal Transduct Targeted Ther* 2023;**8**:293.
4. Jia Y, Jiang Y, He Y, Zhang W, Zou J, Magar KT, et al. Approved nanomedicine against diseases. *Pharmaceutics* 2023;**15**:774.
5. Wilhelm S, Tavares AJ, Dai Q, Ohta S, Audet J, Dvorak HF, et al. Analysis of nanoparticle delivery to tumours. *Nat Rev Mater* 2016;**1**: 16014.
6. Chen H, Kreider W, Brayman AA, Bailey MR, Matula TJ. Blood vessel deformations on microsecond time scales by ultrasonic cavitation. *Phys Rev Lett* 2011;**106**:034301.
7. Sonabend AM, Gould A, Amidei C, Ward R, Schmidt KA, Zhang DY, et al. Repeated blood−brain barrier opening with an implantable ultrasound device for delivery of albumin-bound paclitaxel in patients with recurrent glioblastoma: a phase 1 trial. *Lancet Oncol* 2023;**24**: 509−22.
8. Al Sariri T, Penta R. Multi-scale modelling of nanoparticle delivery and heat transport in vascularised tumours. *Math Med Biol* 2022;**39**: 332−5.
9. May JP, Li SD. Hyperthermia-induced drug targeting. *Expet Opin Drug Deliv* 2013;**10**:511−27.
10. Miller MA, Chandra R, Cuccarese MF, Pfirschke C, Engblom C, Stapleton S, et al. Radiation therapy primes tumors for nanotherapeutic delivery *via* macrophage-mediated vascular bursts. *Sci Transl Med* 2017;**9**:eaal0225.
11. Wei Q, He J, Wang S, Hua S, Qi Y, Li F, et al. Low-dose X-ray enhanced tumor accumulation of theranostic nanoparticles for high-performance bimodal imaging-guided photothermal therapy. *J Nanobiotechnol* 2021;**19**:155.
12. Han X, Wang F, Shen J, Chen S, Xiao P, Zhu Y, et al. Ultrasound nanobubble coupling agent for effective noninvasive deep-layer drug delivery. *Adv Mater* 2023;**36**:e2306993.
13. Schoellhammer CM, Schroeder A, Maa R, Lauwers GY, Swiston A, Zervas M, et al. Ultrasound-mediated gastrointestinal drug delivery. *Sci Transl Med* 2015;**7**:310ra168.
14. Ahmed D, Sukhov A, Hauri D, Rodrigue D, Maranta G, Harting J, et al. Bioinspired acousto-magnetic microswarm robots with upstream motility. *Nat Mach Intell* 2021;**3**:116−24.
15. Wu Y, Liu Y, Huang Z, Wang X, Jin Z, Li J, et al. Control of the activity of CAR-T cells within tumours *via* focused ultrasound. *Nat Biomed Eng* 2021;**5**:1336−47.
16. Ma K, Xu S, Tao T, Qian J, Cui Q, Rehman SU, et al. Magnetosome-inspired synthesis of soft ferrimagnetic nanoparticles for magnetic tumor targeting. *Proc Natl Acad Sci U S A* 2022;**119**:e2211228119.
17. Zakharchenko A, Guz N, Laradji AM, Katz E, Minko S. Magnetic field remotely controlled selective biocatalysis. *Nat Catals* 2018;**1**: 73−81.
18. Tang M, Chen B, Xia H, Pan M, Zhao R, Zhou J, et al. pH-gated nanoparticles selectively regulate lysosomal function of tumour-associated macrophages for cancer immunotherapy. *Nat Commun* 2023;**14**:5888.
19. Gao C, Huang Q, Liu C, Kwong CHT, Yue L, Wan JB, et al. Treatment of atherosclerosis by macrophage-biomimetic nanoparticles *via* targeted pharmacotherapy and sequestration of proinflammatory cytokines. *Nat Commun* 2020;**11**:2622.
20. Wang K, Li Y, Wang X, Zhang Z, Cao L, Fan X, et al. Gas therapy potentiates aggregation-induced emission luminogen-based photoimmunotherapy of poorly immunogenic tumors through cGAS−STING pathway activation. *Nat Commun* 2023;**14**:2950.
21. Weng Y, Chen H, Chen X, Yang H, Chen CH, Tan H. Adenosine triphosphate-activated prodrug system for on-demand bacterial inactivation and wound disinfection. *Nat Commun* 2022;**13**:4712.
22. Wu T, Lang T, Zheng C, Yan W, Li Y, Zhu R, et al. Promote intratumoral drug release and penetration to counteract docetaxel-induced metastasis by photosensitizer-modified red blood cell membrane-coated nanoparticle. *Adv Funct Mater* 2023;**33**:2212109.
23. He Q, Chen J, Yan J, Cai S, Xiong H, Liu Y, et al. Tumor microenvironment responsive drug delivery systems. *Asian J Pharm Sci* 2020; **15**:416−48.
24. Verkhovskii RA, Ivanov AN, Lengert EV, Tulyakova KA, Shilyagina NY, Ermakov AV. Current principles, challenges, and new metrics in pH-responsive drug delivery systems for systemic cancer therapy. *Pharmaceutics* 2023;**15**:1566.
25. Chiang CS, Lin YJ, Lee R, Lai YH, Cheng HW, Hsieh CH, et al. Combination of fucoidan-based magnetic nanoparticles and immunomodulators enhances tumour-localized immunotherapy. *Nat Nanotechnol* 2018;**13**:746−54.
26. Zheng J, Ge H, Zhou D, Yao Q, Long S, Sun W, et al. An activatable prodrug nanosystem for ultrasound-driven multimodal tumor therapy and metastasis inhibition. *Adv Mater* 2023;**35**:e2308205.
27. Xu C, Huang J, Jiang Y, He S, Zhang C, Pu K. Nanoparticles with ultrasound-induced afterglow luminescence for tumour-specific theranostics. *Nat Biomed Eng* 2023;**7**:298−312.
28. Zhao X, Yang CX, Chen LG, Yan XP. Dual-stimuli responsive and reversibly activatable theranostic nanoprobe for precision tumor-targeting and fluorescence-guided photothermal therapy. *Nat Commun* 2017;**8**:14998.
29. Park J, Zhang Y, Vykhodtseva N, Jolesz FA, McDannold NJ. The kinetics of blood brain barrier permeability and targeted doxorubicin delivery into brain induced by focused ultrasound. *J Control Release* 2012;**162**:134.
30. Park J, Aryal M, Vykhodtseva N, Zhang YZ, McDannold N. Evaluation of permeability, doxorubicin delivery, and drug retention in a rat brain tumor model after ultrasound-induced blood-tumor barrier disruption. *J Control Release* 2017;**250**:77−85.
31. Arsiwala TA, Sprowls SA, Blethen KE, Adkins CE, Saralkar PA, Fladeland RA, et al. Ultrasound-mediated disruption of the blood tumor barrier for improved therapeutic delivery. *Neoplasia* 2021;**23**: 676−91.
32. Tharkar P, Varanasi R, Wong WSF, Jin CT, Chrzanowski W. Nano-enhanced drug delivery and therapeutic ultrasound for cancer treatment and beyond. *Front Bioeng Biotechnol* 2019;**7**:324.
33. Liao M, Chen F, Chen L, Wu Z, Huang J, Pang H, et al. Synergistic enzyme-mimetic catalysis-based non-thermal sonocavitation and

sonodynamic therapy for efficient hypoxia relief and cancer ablation. *Small* 2023;**19**:e2302744.
34. Du L, Zhang H, Wang Z, Zhuang T, Wang Z. Boosting the electrochemiluminescence of luminol by high-intensity focused ultrasound pretreatment combined with 1T/2H MoS_2 catalysis to construct a sensitive sensing platform. *Ultrason Sonochem* 2023;**92**:106264.
35. Kim G, Wu Q, Chu JL, Smith EJ, Oelze ML, Moore JS, et al. Ultrasound controlled mechanophore activation in hydrogels for cancer therapy. *Proc Natl Acad Sci U S A* 2022;**119**:e2109791119.
36. Suehiro S, Ohnishi T, Yamashita D, Kohno S, Inoue A, Nishikawa M, et al. Enhancement of antitumor activity by using 5-ALA-mediated sonodynamic therapy to induce apoptosis in malignant gliomas: significance of high-intensity focused ultrasound on 5-ALA-SDT in a mouse glioma model. *J Neurosurg* 2018;**129**:1416.
37. Yu X, Li X, Chen Q, Wang S, Xu R, He Y, et al. High intensity focused ultrasound-driven nanomotor for effective ferroptosis-immunotherapy of TNBC. *Adv Sci* 2024;**11**:e2305546.
38. Jiang X, Stockwell BR, Conrad M. Ferroptosis: mechanisms, biology and role in disease. *Nat Rev Mol Cell Biol* 2021;**22**:266−82.
39. Kuang F, Liu J, Tang D, Kang R. Oxidative damage and antioxidant defense in ferroptosis. *Front Cell Dev Biol* 2020;**8**:586578.
40. Hasan AA, Kalinina E, Tatarskiy V, Shtil A. The thioredoxin system of mammalian cells and its modulators. *Biomedicines* 2022;**10**:1757.
41. Oberacker T, Kraft L, Schanz M, Latus J, Schricker S. The importance of thioredoxin-1 in health and disease. *Antioxidants* 2023;**12**:1078.
42. Demelash A, Pfannenstiel LW, Liu L, Gastman BR. Mcl-1 regulates reactive oxygen species *via* NOX4 during chemotherapy-induced senescence. *Oncotarget* 2017;**8**:28154−68.
43. Hu CM, Fang RH, Wang KC, Luk BT, Thamphiwatana S, Dehaini D, et al. Nanoparticle biointerfacing by platelet membrane cloaking. *Nature* 2015;**526**:118−21.
44. Tan H, Song Y, Chen J, Zhang N, Wang Q, Li Q, et al. Platelet-like fusogenic liposome-mediated targeting delivery of miR-21 improves myocardial remodeling by reprogramming macrophages post myocardial ischemia−reperfusion injury. *Adv Sci* 2021;**8**:e2100787.
45. Wang HL, Zhu YF, Zhang LL, Liu HW, Liu CY, Zhang B, et al. Nanoplateletsomes for rapid hemostasis performance. *Chin Chem Lett* 2022;**33**:2937−40.
46. Liu C, Ruan S, He Y, Li X, Zhu Y, Wang H, et al. Broad-spectrum and powerful neutralization of bacterial toxins by erythroliposomes with the help of macrophage uptake and degradation. *Acta Pharm Sin B* 2022;**12**:4235−49.
47. Zhang L, Zhu Y, Wei X, Chen X, Li Y, Zhu Y, et al. Nanoplateletsomes restrain metastatic tumor formation through decoy and active targeting in a preclinical mouse model. *Acta Pharm Sin B* 2022;**12**:3427−39.
48. O'Donnell VB, Murphy RC, Watson SP. Platelet lipidomics: modern day perspective on lipid discovery and characterization in platelets. *Circ Res* 2014;**114**:1185.
49. Molinaro R, Corbo C, Martinez JO, Taraballi F, Evangelopoulos M, Minardi S, et al. Biomimetic proteolipid vesicles for targeting inflamed tissues. *Nat Mater* 2016;**15**:1037−46.
50. Gevertz JL, Kareva I. Guiding model-driven combination dose selection using multi-objective synergy optimization. *CPT Pharmacometrics Syst Pharmacol* 2023;**12**:1698−713.
51. Chou TC. Drug combination studies and their synergy quantification using the Chou-Talalay method. *Cancer Res* 2010;**70**:440−6.
52. McFarlane S, Coulter JA, Tibbits P, O'Grady A, McFarlane C, Montgomery N, et al. CD44 increases the efficiency of distant metastasis of breast cancer. *Oncotarget* 2015;**6**:11465.
53. Alves CS, Burdick MM, Thomas SN, Pawar P, Konstantopoulos K. The dual role of CD44 as a functional P-selectin ligand and fibrin receptor in colon carcinoma cell adhesion. *Am J Physiol Cell Physiol* 2008;**294**:C907−16.
54. Smith SM, Lyu YL, Cai L. NF-κB affects proliferation and invasiveness of breast cancer cells by regulating CD44 expression. *PLoS One* 2014;**9**:e106966.
55. Zhang J, Yamada O, Kida S, Matsushita Y, Yamaoka S, Chagan-Yasutan H, et al. Identification of CD44 as a downstream target of noncanonical NF-κB pathway activated by human T-cell leukemia virus type 1-encoded tax protein. *Virology* 2011;**413**:244−52.
56. Marotta LL, Almendro V, Marusyk A, Shipitsin M, Schemme J, Walker SR, et al. The JAK2/STAT3 signaling pathway is required for growth of $CD44^+CD24^-$ stem cell-like breast cancer cells in human tumors. *J Clin Investig* 2011;**121**:2723−35.
57. Liu JX, Jia BY, Li ZB, Li WL. Reactive oxygen species-responsive polymer drug delivery systems. *Front Bioeng Biotechnol* 2023;**11**:1115603.
58. Wang P, Gong Q, Hu J, Li X, Zhang X. Reactive oxygen species (ROS)-responsive prodrugs, probes, and theranostic prodrugs: applications in the ros-related diseases. *J Med Chem* 2021;**64**:298.
59. Maeda M, Muragaki Y, Okamoto J, Yoshizawa S, Abe N, Nakamoto H, et al. Sonodynamic therapy based on combined use of low dose administration of epirubicin-incorporating drug delivery system and focused ultrasound. *Ultrasound Med Biol* 2017;**43**:2295−301.
60. Läubli H, Borsig L. Selectins promote tumor metastasis. *Semin Cancer Biol* 2010;**20**:169−77.
61. Gay LJ, Felding-Habermann B. Contribution of platelets to tumour metastasis. *Nat Rev Cancer* 2011;**11**:123−34.
62. Schlesinger M. Role of platelets and platelet receptors in cancer metastasis. *J Hematol Oncol* 2018;**11**:125.
63. Sasaki T, Shirai T, Tsukiji N, Otake S, Tamura S, Ichikawa J, et al. Functional characterization of recombinant snake venom rhodocytin: Rhodocytin mutant blocks CLEC-2/podoplanin-dependent platelet aggregation and lung metastasis. *J Thromb Haemostasis* 2018;**16**:960−72.
64. Braun A, Anders HJ, Gudermann T, Mammadova-Bach E. Platelet-cancer interplay: molecular mechanisms and new therapeutic avenues. *Front Oncol* 2021;**11**:665534.
65. Park J, Zhang Y, Vykhodtseva N, Jolesz FA, McDannold NJ. The kinetics of blood brain barrier permeability and targeted doxorubicin delivery into brain induced by focused ultrasound. *J Control Release* 2012;**162**:134−42.
66. Eranki A, Srinivasan P, Ries M, Kim A, Lazarski CA, Rossi CT, et al. High-intensity focused ultrasound (HIFU) triggers immune sensitization of refractory murine neuroblastoma to checkpoint inhibitor therapy. *Clin Cancer Res* 2020;**26**:1152−61.
67. Hu Z, Yang XY, Liu Y, Morse MA, Lyerly HK, Clay TM, et al. Release of endogenous danger signals from HIFU-treated tumor cells and their stimulatory effects on APCs. *Biochem Biophys Res Commun* 2005;**335**:124−31.
68. Rosberger DF, Coleman DJ, Silverman R, Woods S, Rondeau M, Cunningham-Rundles S. Immunomodulation in choroidal melanoma: reversal of inverted CD4/CD8 ratios following treatment with ultrasonic hyperthermia. *Biotechnol Therapeut* 1994;**5**:59−68.
69. Hynynen K, McDannold N, Vykhodtseva N, Jolesz FA. Noninvasive MR imaging-guided focal opening of the blood−brain barrier in rabbits. *Radiology* 2001;**220**:640−6.